



**HAL**  
open science

# Experimental sensitivity analysis of the global properties of a 2D turbulent wake

Vladimir Parezanovic, Olivier Cadot

► **To cite this version:**

Vladimir Parezanovic, Olivier Cadot. Experimental sensitivity analysis of the global properties of a 2D turbulent wake. *Journal of Fluid Mechanics*, 2012, 693, pp.115-149. hal-01289905

**HAL Id: hal-01289905**

**<https://ensta-paris.hal.science/hal-01289905v1>**

Submitted on 17 Mar 2016

**HAL** is a multi-disciplinary open access archive for the deposit and dissemination of scientific research documents, whether they are published or not. The documents may come from teaching and research institutions in France or abroad, or from public or private research centers.

L'archive ouverte pluridisciplinaire **HAL**, est destinée au dépôt et à la diffusion de documents scientifiques de niveau recherche, publiés ou non, émanant des établissements d'enseignement et de recherche français ou étrangers, des laboratoires publics ou privés.

# Experimental sensitivity analysis of the global properties of a 2D turbulent wake

VLADIMIR PAREZANOVIĆ<sup>†</sup> AND OLIVIER CADOT

Unité de Mécanique, École Nationale Supérieure de Techniques Avancées de ParisTech,  
Chemin de la Hunière, 91761 Palaiseau, France

(Received 9 September 2011)

The sensitivity of the global properties of a 2D turbulent wake produced by the separated flow of a "D" shaped cylinder at  $Re = 13000$  is investigated experimentally using a small circular control cylinder as a local disturbance. The height of the main cylinder is  $D = 25\text{mm}$  and control cylinders are of diameters  $d = 0.04D$  and  $d = 0.12D$ ; the former being smaller than the shear layers thickness detaching from the main cylinder, while the latter is larger. In both cases, the control cylinder is able to modify the global frequency, base pressure and spanwise velocity correlation. The results are presented as sensitivity maps. Reynolds stresses spatial structure and the recirculation bubble length are examined in detail when the control cylinder is displaced vertically across the wake at a fixed downstream location. It is found that the increase of the recirculation bubble length is accompanied by a damping of Reynolds stresses with a downstream shift of their spatial structures together with the base pressure increase. The global frequency can be either decreased or increased independently of the bubble length modification. The sensitivity of these global properties are interpreted on the basis of the ability of the control cylinder to change the size of the formation region of the Kármán vortex street by interacting with the primary detached shear layers. The corresponding physical mechanisms are discussed. The impact of a 2D control cylinder on the 3D properties of the wake is examined through spanwise correlation. This is found to be improved whenever the control cylinder is placed inside the recirculation region of the main cylinder wake.

## 1. Introduction

The seminal work of Strykowski & Sreenivasan (1985, 1990) investigates the flow around a circular cylinder disturbed by a much smaller secondary cylinder in the neighborhood of the first instability threshold. For certain locations of the secondary cylinder the authors find a wake stabilization effect systematically accompanied by a global frequency reduction that could go toward the complete unsteadiness suppression. Their results are represented in terms of spatial sensitivity map showing the regions around the primary cylinder in which the global mode instability is mostly affected. They proposed a stabilization mechanism based on the interaction and modification of the shear layers in the frame of the model of Gerrard (1966), although the physical mechanism involves vortex shedding at larger Reynolds numbers. Since then, numerous studies have investigated this flow at about the same Reynolds number but only for the most effective positions of the control cylinder that suppress vortex shedding. The numerical simulations of Mittal (2001) and Mittal & Raghuvanshi (2001) at  $Re = 100$  are in fairly good

<sup>†</sup> Present address: Unité de Mécanique, ENSTA-ParisTech, Chemin de la Hunière, Palaiseau, France.

agreement with the Strykowski & Sreenivasan (1985, 1990) results. The authors argued that a favorable pressure gradient locally introduced by the control cylinder might stabilize one of the shear layers. The consequences of this passive control on drag and lift have been studied numerically and experimentally by Dalton *et al.* (2001) for larger, but still moderate Reynolds numbers of 100 to 3000 where mean drag and fluid force fluctuations are found to be reduced. The recent numerical study of Yildirim *et al.* (2010) at  $Re = 80$  also confirms the force reduction. In addition, it shows how the vorticity introduced by the secondary cylinder in the vicinity of the shear layers of the primary cylinder affects vortex dynamics and vortex arrangements in its wake. Kuo *et al.* (2007) have performed numerical investigation of a configuration with two small cylinders in the wake at  $Re$  from 80 to 300. They also observed wake stabilization with associated reduction in fluctuating aerodynamic forces. In both Strykowski & Sreenivasan (1990) and Kuo *et al.* (2007), flow displacement from the outside flow into the recirculation region due to the presence of the control cylinder(s) is observed.

On the theoretical background, the effects of a local perturbation on the global mode of 2D wakes (Hill 1992; Chomaz 2005) has received much attention since the work of Giannetti & Luchini (2007); Luchini *et al.* (2008). For Reynolds number close to the first instability ( $Re < 150$ ), the computation of the direct and adjoint global modes of the base flow is able to retrieve the spatial structure of the sensitivity (later referred as sensitivity map) of the Bénard von Kármán instability obtained experimentally by Strykowski & Sreenivasan (1985, 1990). Recent theoretical developments (Luchini *et al.* 2008; Marquet *et al.* 2008; Luchini *et al.* 2009; Pralits *et al.* 2010) have shown that the basic flow modification introduced by the local perturbation represents the dominant contribution to the global mode sensitivity. The theory offers new tools for aerodynamicist to predict optimal location for flow modification. However, at the present stage it only concerns flows at low Reynolds numbers near the threshold of a global instability. For the numerous industrial applications of large Reynolds flows, one may ask whether similar theoretical development can be made for flows that are still governed by global mode dynamics. Such attempts for compressible flows have been successfully investigated by Crouch *et al.* (2009), which gives hopes for this research field.

Experimentally, the method of introducing a small control cylinder is very successful in reducing forces for large Reynolds number flows. Sakamoto *et al.* (1991) and Sakamoto & Haniu (1994) investigated in detail the method applied to square and circular primary cylinders for  $Re > 10\,000$ . Similarly to Strykowski & Sreenivasan (1985, 1990), their results are displayed in sensitivity maps of global quantities such as drag, lift, and Strouhal numbers. For certain positions of the control cylinder the drag can be reduced by up to 40% for the circular cylinder and 30% for the square cylinder and the global frequency can be either increased or decreased. The differences between the two geometries are essentially due to the additional degree of freedom introduced by the separation point displacements that are only possible for the circular cylinder. When the separation points are fixed, which is the case for the square cylinder, the maximum reduction occurs when the control cylinder is located near the outer boundary of the separated shear layer in the vicinity of the bluff body. This position at large  $Re$  is very similar to the position for shedding suppression observed at low Reynolds number by Strykowski & Sreenivasan (1990). All of these effects for large Reynolds numbers recall previous studies concerning bluff body wakes controlled with splitter plates Roshko (1954), Bearman (1965) and Apelt *et al.* (1973); Apelt & West (1975). The splitter plate placed on the symmetry axes at the rear of the main body modifies the coupling of the opposite shear layers. The base pressure is drastically increased and consequently the drag reduced (by almost 30%) and the global frequency can be affected by about +30% to -50% depending on the

cylinder's shape (Apelt & West 1975). While splitter plates are generally very intrusive, small control cylinders, similar to local 2D steady disturbances, lead to the same order of magnitude for the global quantities modifications. In the works of Sakamoto *et al.* (1991); Sakamoto & Haniu (1994), the wake topologies have not been studied in detail and some positions of the control cylinder related to the region inside the recirculating bubble have not been explored. In order to avoid the effect of flow reattachment on the primary bluff body, Thiria *et al.* (2009) investigated the controlled wake at large Reynolds number of a "D" shaped cylinder. Their study was restricted to the position of the control cylinder for which drag is substantially reduced. They found the maximum of the global mode spatial structure, called "the global mode envelope" in Zielinska & Wesfreid (1995), to be strongly inhibited and shifted downstream. Similarly to Sakamoto *et al.* (1991), the effect on the base pressure of one and two control cylinders in the "D" cylinder wake have been investigated in Cadot *et al.* (2009). For the optimum position of the control cylinder that produces the maximum increase of base pressure (reduction of drag), it is found that there is an optimal position for a second control cylinder, which is able to further increase the base pressure (to additionally reduce drag). The global mode envelope is shifted downstream more than in the case of one control cylinder. The analysis of the sensitivity of the global mode frequency of the "D" cylinder wake to the position of a single control cylinder has been studied by Parezanović & Cadot (2009a). Sensitivity map displays different regions presenting distinctive mechanisms of frequency selection. A striking difference compared to the sensitivity analysis at low  $Re$  (Strykowski & Sreenivasan 1985, 1990; Giannetti & Luchini 2007; Luchini *et al.* 2008; Marquet *et al.* 2008; Luchini *et al.* 2009), for which the global frequency is always decreased (compared to that of the undisturbed case) is that at large  $Re$  the extinction of vortex shedding can be either accompanied by a low or high global mode frequency.

The present article aims at clarifying the effect of the local 2D disturbance in a turbulent wake of a cylinder, in order to understand the origin of the global properties sensitivity. Using the same experimental set-up as Parezanović & Cadot (2009a), we are investigating the nature of mechanisms responsible for the modification of the global mode and its relationship to the mean flow modification. The novelties from the letter of Parezanović & Cadot (2009a) are: firstly, the use of a smaller control cylinder, that can be better associated to the term "disturbance"; secondly, a sensitivity analysis of the spatial structure of the Reynolds stresses is performed; thirdly, the 3D properties of the disturbed turbulent wake are investigated. Especially, we try to answer the following questions: why is the global mode spatial structure shifted downstream and damped? How to explain the frequency change and the drag reduction? How do these effects behave, as the control cylinder diameter decreases? What are the consequences of the steady 2D disturbance on the 3D properties of the wake?

The structure of the article will be the following: we will first present the experimental setup and measurement equipment in section 2. The results will be presented in section 3, first for the natural flow, and then for the controlled wake in terms of global mode frequency measurements, PIV measurements as global mode envelope characterization, base pressure measurements and two-point velocity correlation in the spanwise direction. We propose some physical mechanisms in the discussion (section 4) that are involved in the sensitivity of the global mode envelope and frequency to the presence of the 2D disturbance. A drag reduction mechanism is also described. The paper finalizes with a brief recapitulation and conclusion in section 5.

## 2. Experimental setup and measurements

### 2.1. Geometry

The experimental investigation uses an open circuit wind tunnel of Eiffel type. The dimensions of the test area are  $400\text{mm} \times 400\text{mm}$  with open sides. As can be seen in figure 1(a), the metal bluff body model is fixed at the edges of its span to the floor of the wind tunnel. The span of the body is  $S = 600\text{mm}$ . Its cross section is an elongated "D" shape of height  $D = 25\text{mm}$  and length of  $L = 2D = 50\text{mm}$ . The secondary (control) cylinder has a circular cross-section, and two different diameters are used:  $d = 1\text{mm}$  and  $d = 3\text{mm}$ . In both cases the span of the control cylinder is  $800\text{mm}$  and it is fixed to a metal frame which is connected to the displacement console. Axial tension is applied to the control cylinders in order to avoid flow induced vibrations. The absence of vibrations is visually confirmed by a high speed camera. The metal frame supporting the control cylinder does not obstruct the flow since it is located on the sides of the tunnel outside of the steady flow and below the tunnel floor. The supporting frame is connected to three Newport (M-)MTM long travel consoles which are controlled by the Newport Motion Controller ESP301. For the purposes of this study, the control cylinder is displaced only in  $Ox$  and  $Oy$  directions. The displacement console is capable of positioning the control cylinder with an accuracy better than  $0.1\text{mm}$ . The flow conditions of the experiment are defined by a free stream velocity of  $U_0 = 8\text{m/s}$  measured at the inlet of the tunnel test area. The Reynolds number of the flow based on  $D = 25\text{mm}$  is calculated to be  $Re \approx 13000$ . The results of the experiments are obtained from hot wire probe anemometry and the PIV of the flow. Details of each measurement will be presented in the following sections.

### 2.2. Displacement of the control cylinder

The experiments are performed by moving the control cylinder through a set of pre-determined positions  $(x_c, y_c)$ , and measuring local velocity in the wake and pressure distribution on the main cylinder for each position. The rectangular area investigated extends  $1.8D$  downstream from the base of the bluff body and  $\pm 1.1D$  above and below the horizontal axis of symmetry of the bluff body. The control cylinder is displaced in  $0.04D(1\text{mm})$  steps in the horizontal direction and in  $0.02D(0.5\text{mm})$  steps in the vertical direction. The movement sequence of the control cylinder is as follows: from the starting position  $(x_c = 0, y_c = -1.1D)$  the control cylinder is moved through 111 steps in the  $+Oy$  direction then by 1 step in  $+Ox$  direction continued by 111 steps in the  $-Oy$  direction and finally by 1 step in  $+Ox$  direction. This pattern is repeated so as to cover the area of interest of  $1.8D \times 2.2D$  with a resolution of  $45 \times 111$  positions of the control cylinder. At each position, the control cylinder remains stationary for a specified time interval during which measurements are obtained. The whole experiment, taking into account short delays between the starting and stopping of the movement (for each step) and the measurements, lasts 48 hours.

### 2.3. Local velocity measurements

Figure 1(b) shows the placement of the three hot wire probes, marked  $A0$  through  $A2$ , in the wake. The hot wire probes measure the modulus of local velocity in the  $xOy$  plane and will be denoted as  $u_{Ai}(t)$  where  $i$  refers to the label of the hot wire probe. They are all located at  $x = 6D$  downstream of the trailing edge of the main cylinder and at the same vertical level as its lower horizontal edge at  $y = -0.5D$ . They are located at  $z = -2D$ ,  $z = 0$  and  $z = +2D$  in the spanwise direction.

We use three DISA 55M10 hot wire anemometry measurement units connected to a

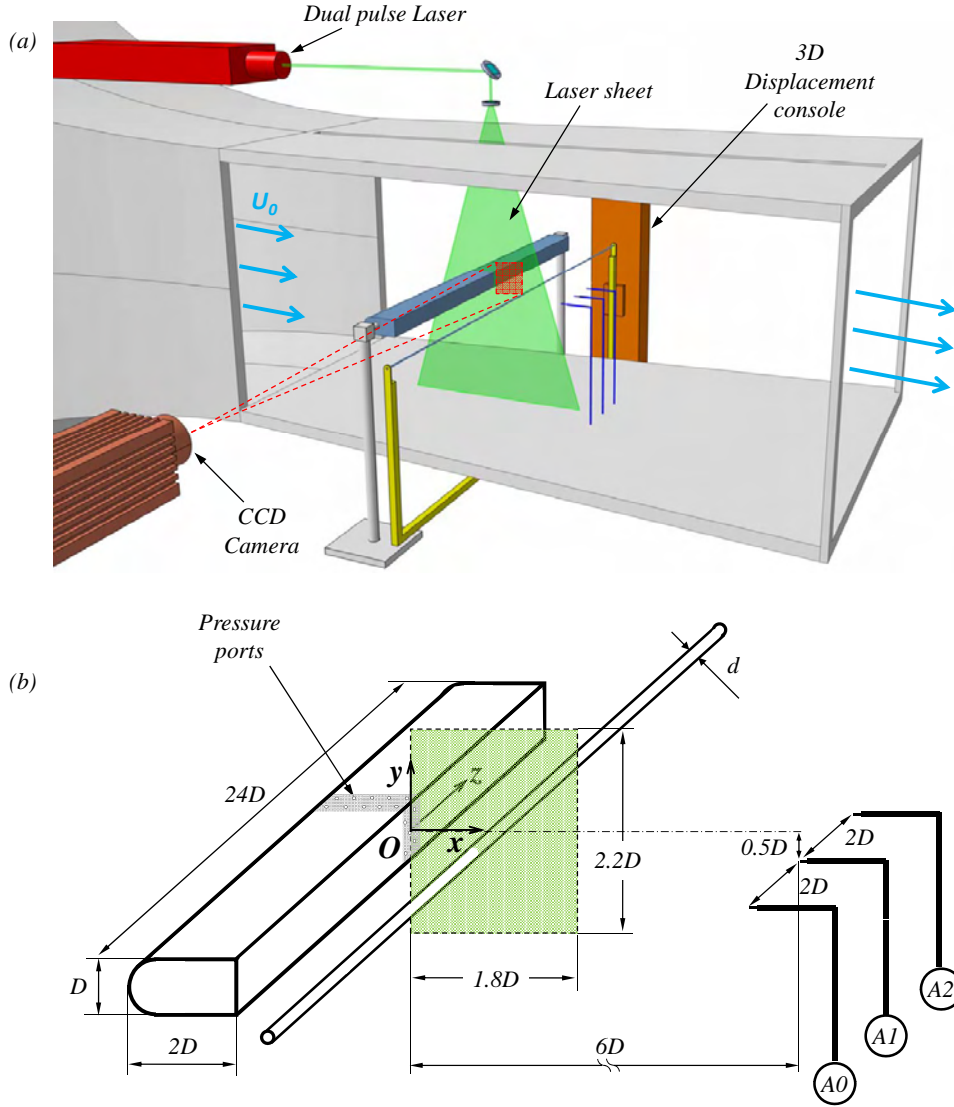


FIGURE 1. The experimental apparatus consisting of the fixed "D"-shaped main cylinder and a circular control cylinder connected to the displacement console and movable in  $xOy$  plane. The measurements system comprises of three hot wire probes, a differential pressure measurement system, and a PIV acquisition system.

PC with Labview software as the control platform to perform simultaneous acquisition of the signals. The wire probes are DANTEC and use an overheat ratio of 1.5. The acquisition of each velocity signal is performed at a rate of  $1kHz$  for  $30s$ . The power spectra  $P_{u_{Ai}}(f) = \frac{1}{2\pi} \int \langle u_{Ai}(t)u_{Ai}(t + \tau) \rangle_T \exp(-2\pi if\tau) d\tau$  computed from the velocity time series are averaged over a window of  $T = 4$  seconds. Hence, the frequency resolution of the spectra is  $\Delta f = 0.25Hz$ . In order to find the frequency of the global mode, we use the peak detection subroutine, based on an algorithm that fits a quadratic

polynomial to sequential groups of data points, where a group of points corresponds to a bandwidth of  $10Hz$ .

In order to characterize the 3D structure of the wake, spatial correlations are obtained from cross correlations between the three local velocity measurements. The measurements of hot wire probes  $A0$ ,  $A1$  and  $A2$  are used to compute three spanwise correlation coefficients:  $r_{[0-1]}$ ,  $r_{[1-2]}$ ,  $r_{[0-2]}$  defined as:

$$r_{[i-j]} = \frac{\overline{u'_{Ai}u'_{Aj}}}{\sqrt{\overline{u'^2_{Ai}} \overline{u'^2_{Aj}}}}, \quad (2.1)$$

where primes denote the fluctuating part of the velocity following the classical Reynolds decomposition  $X'(t) = X(t) - \overline{X}$ . This notation will be used throughout the article.

#### 2.4. PIV measurements

Particle Image Velocimetry is used to visualize and obtain the velocity field around the bluff body and the control cylinder. The system comprises a Litron LP4550 dual pulse  $200mJ$  Nd:YAG laser and a Lavision Imager PRO camera. The setup acquires images at a rate of  $11Hz$  and Lavision software Davis 7 has been used to calculate the velocity fields. The vector calculation is done using single-pass, dual frame cross-correlation on constant window size. The interrogation window size is  $32 \times 32$  pixels and the entire image is  $1600 \times 1400$  pixels. The time delay between the two frames is  $75\mu s$  for both experiments. Each acquisition records 200 image pairs.

The data from our PIV measurements will be presented in the form of: i) component of mean velocity in  $Ox$  direction  $\overline{u}(x, y)$ , ii) mean vorticity component in  $xOy$  plane  $\overline{\omega}_z(x, y) = \overline{(\frac{\partial v}{\partial x} - \frac{\partial u}{\partial y})}$ , iii) Reynolds stress components  $\overline{v'^2}(x, y)$  and  $\overline{u'v'}(x, y)$ .

We will use  $\overline{u}(x, y)$  to measure the length of the recirculation bubble  $L_b/D$  as the horizontal distance from the trailing edge of the main cylinder to the point where the iso-contour of  $\overline{u} = 0$  intersects  $Ox$ . The uncertainty of the  $L_b/D$  is measured manually from stagnation point definition of the velocity field streamlines.

#### 2.5. Pressure measurements

The main cylinder is equipped with 32 pressure taps (see figure 1b) distributed along the entire perimeter of its cross-section at mid-span ( $z = 0$ ). They are connected to two Scanivalve DSA 3217/16px differential pressure measurement arrays capable of taking 100 samples of pressure per second. These samples are automatically averaged and a mean pressure is given as an output. In our mapping experiments, we have performed 40s long measurements of pressure for each position of the control cylinder. From these measurements, we obtain a mean pressure coefficient  $C_p(s)$ :

$$C_p(s) = \frac{p(s) - p_{ref}}{p(0) - p_{ref}}, \quad (2.2)$$

where  $p_{ref}$  is a reference static pressure measured at the inlet of the wind tunnel test area and  $p(0)$  is the pressure measured at the head of the main cylinder. The sectional form drag  $C_D$  is then classically estimated by integrating the projected pressure stress over the cylinder perimeter:

$$C_D = \frac{1}{D} \oint C_p(s) \vec{n} \cdot \vec{e}_x ds. \quad (2.3)$$

The base pressure coefficient  $C_{pb}$  is computed from the spatial average of the 5 pressure taps that are distributed on the blunt base of the cylinder:

$$C_{pb} = \frac{1}{D} \int_{base} C_p(s) ds. \quad (2.4)$$

The DSA devices are not able to recover the true rate of fluctuation of the pressure but we can still build the  $C_{pbRMS}$  from those 40s of measurements which gives an image of the fluctuation levels.

### 3. Results

#### 3.1. The natural case

We first characterize the flow around the main body without any control cylinder. Figures 2 and 3 summarize the main properties of the natural flow. The color map in figure 2(a) shows the instantaneous modulus of velocity obtained from PIV acquisitions at  $z = 0$ . The boundary layer, which is initiated at the stagnation point  $x = -2D$  separates at the junction with the flat wall at  $x = -1.5D$ . The laminar separation becomes turbulent, as shown by the presence of periodic regions of high velocities in figure 2(a) revealing a transition mechanism due to the Kelvin-Helmholtz instability. The detached boundary layer re-attaches at about  $x = -0.4D$ . The turbulent boundary layer finally breaks away at the sharp trailing edge  $x = 0$  of the main body. From hot-wire probe measurements of the boundary layer at  $x = -0.1mm$ , just upstream of the trailing edge, we have obtained a boundary layer thickness of  $\delta_{99} = 0.12$ , a momentum deficit thickness of  $\delta_2 = 0.014$  and a form factor of  $H_{12} = 1.24$ . The boundary layer properties are similar to the compiled results in the recent work of Pastoor *et al.* (2008) involving blunt trailing edge cylinders. However, the base pressure in our case  $C_{pbn} = -0.60$  is lower when compared to previous studies (-0.57 to -0.51). The difference might be attributed to end conditions which are free in our case and bounded by walls in Pastoor *et al.* (2008). The form drag computed from equation 2.3) is  $C_{Dn} = 0.74$ .

The properties of the turbulent mixing layers just after the detachment from the trailing edge are analyzed using flying hot wire measurements performed at  $x = 0.1mm$  and traversed in the vertical direction through  $-2D < y < +2D$  (in steps of  $0.02D$ ). The curves in figure 2(b) show the mean velocity profile,  $\bar{u}_A$  (thick black line); and the fluctuation profile,  $\sigma = \sqrt{\overline{u_A'^2}}$  (dashed line). The maximum fluctuation rate in the mixing layer is 25%. The turbulent mixing layer thickness  $\delta_{1/2}$  can be deduced from the vertical gradient of the mean velocity  $\frac{\partial \bar{u}_A}{\partial y}$ . This gradient is shown as a thin black line in the inset of figure 2(b). Defining  $\delta_{1/2}$  as the width of the velocity gradient peak at half of its height, we find a turbulent layer thickness of  $\delta_{1/2} = 0.05D = 1.25mm$ . The vertical component of the velocity being negligible at the trailing edge, the mean velocity gradient there is also a good estimate of the mean vorticity:  $\frac{\partial \bar{u}_A}{\partial y} \approx \bar{\omega}_z$ . Mean vorticity profile  $\bar{\omega}_z$  measured by PIV is represented with circles in the inset of figure 2(b). If we compare the two curves in the inset we can see that the PIV interrogation window, with its size of  $0.04D \times 0.04D$  induces a clear coarse graining effect. It is clear that the PIV resolution is not accurate enough to measure velocity distribution in shear layers. The PIV measurements will be usefully exploited in a comparative manner between the different flow configurations defined by the control cylinder position.

Now that we have described the flow in the vicinity of the body we turn to some properties of the wake. The mean wake consists of a recirculation bubble shown in figure 2(c). This is a region of reversed flow bounded by the two detached turbulent shear layers



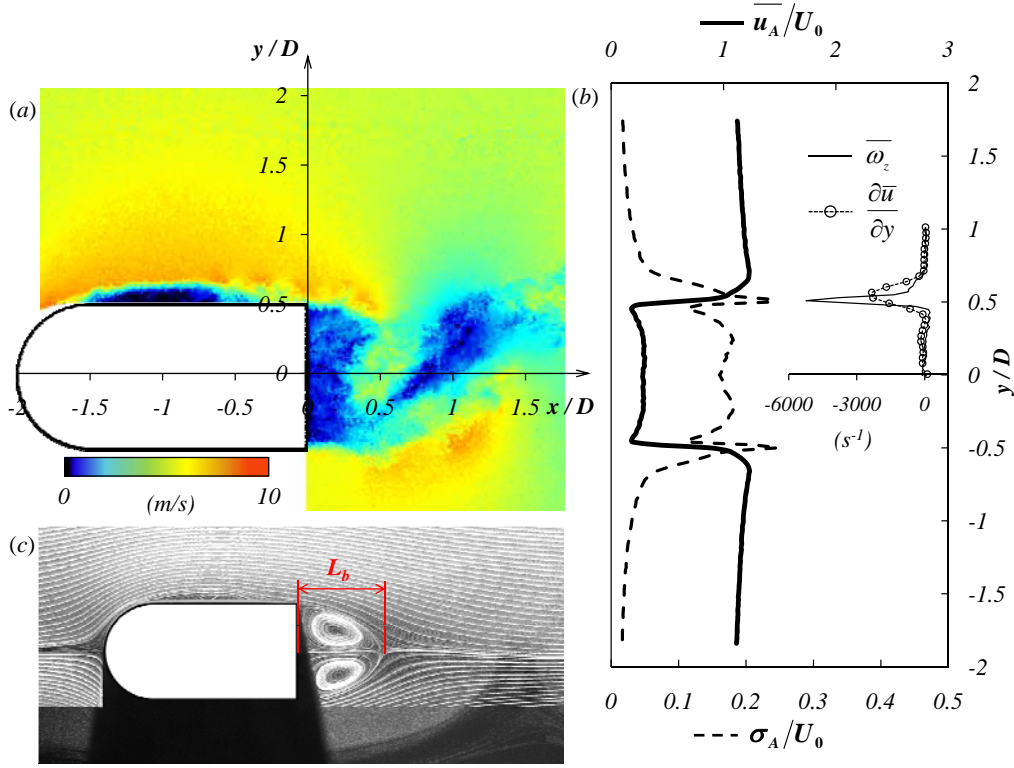


FIGURE 2. Natural flow around the bluff body at  $Re = 13000$ ; the color map (a) shows an instantaneous field of the modulus  $\sqrt{u^2 + v^2}$  with velocities ranging from  $0\text{m/s}$  for black up to  $10\text{m/s}$  for orange. The diagram on the right (b) depicts the vertical profile measured with the flying hot wire just behind the rear of the blunt body at  $x = 0.1\text{mm}$ . The mean  $\bar{u}_A$  (thick line) and the fluctuation  $\sigma$  of velocity (dashed line) are normalized by  $U_0$ . The inset diagram in (b) is a plot of the vorticity  $\bar{\omega}_z$  measured from PIV (circles) and estimated (see text) from local velocity measurements (thin line). The plot shares the primary  $y/D$  axis. (c) recirculation bubble visualized by streamlines of the mean velocity of 500 frames of PIV.

described above and the vortex formation region produced by the shear layers roll-up. A characteristic size of the formation region is the mean bubble length, measured to be  $L_{bn}/D = 0.82 \pm 0.04$  in the case of the natural flow.

The wake dynamics are dominated by a global mode, known as the Kármán vortex street. The detached shear layers roll up and meet each other at a characteristic distance downstream from the trailing edge of the main cylinder, and vortices are shed at a selected frequency. The mean Reynolds stress components  $\overline{v'^2}$  and  $\overline{u'v'}$  obtained from PIV measurements are used to characterize the properties of the vortex formation region. Figure 3(a) and (b) defines some characteristic values, such as the streamwise location of the Reynolds stress extrema  $X_{\overline{v'^2}Max}$ ,  $X_{\overline{u'v'}Max}$  and  $X_{\overline{u'v'}Min}$  whose spatial definitions,  $\delta_{\overline{v'^2}}$  and  $\delta_{\overline{u'v'}}$  are simply estimated from the typical size at about  $(1\text{m/s})^2$  below the value of the extremum which corresponds to the size of the first contour around the extremum in Figure 3. These spatial definitions are used to build error bars in figures 11 and 12.

The global mode frequency is clearly observed in the spectra of the three wire probes in figure 4 by the peaks in amplitude around the same frequency. This is identified as

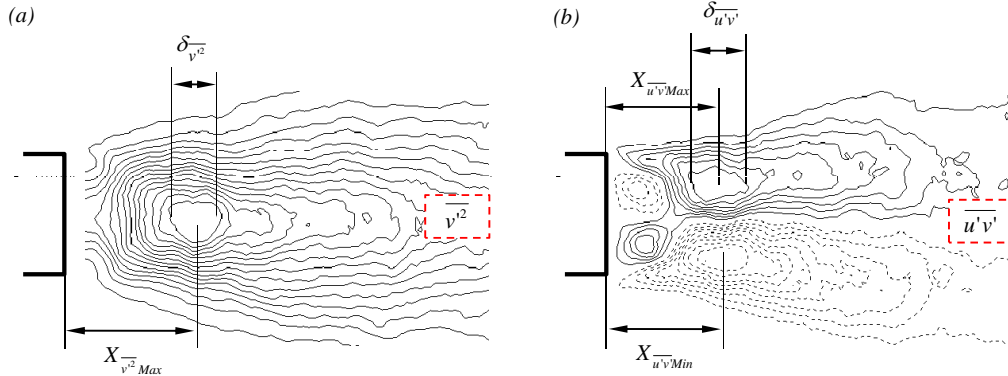


FIGURE 3. Reynolds stress components for the natural flow: (a)  $\overline{v'^2}$  in range of  $0(m/s)^2$  to  $15(m/s)^2$  and (b)  $\overline{u'v'}$  in range of  $\pm 5(m/s)^2$ . The isolines are in the interval of  $1(m/s)^2$  (continuous lines for positive and dashed for negative values).

the natural frequency of  $f_n = 70.75 \pm 0.25 Hz$ . The large width of the peaks are related to the three dimensional disturbances of the turbulent wake, such as oblique vortex shedding and vortex dislocations (Williamson 1996a; Prasad & Williamson 1997). The natural Strouhal number is calculated as  $St = \frac{f_n D}{U_0} = 0.221$ . Between the three spectra obtained at different spanwise locations, we can observe slight differences: the peak of the centerline wire (A1) has larger amplitude, and better definition. The peak of the first harmonic is better seen in the spectra of the wires on the left (A2) and right (A0) of the centerline. The differences in the peak definition are also indicating 3D properties of the wake, partly induced by the ends effect. The similarity of the spectra (A2) and (A0) is a consequence of the experimental symmetry with respect to the central plane  $z = 0$ .

The correlation coefficient values computed from Eq.2.1 for the natural case are  $r_{n[0-1]} = 0.204$ ,  $r_{n[1-2]} = 0.190$ ,  $r_{n[0-2]} = 0.089$ . Three-dimensionality disturbances of the wake have direct impact on the spanwise correlation (Norberg 2001). The correlation values of  $r_{n[0-1]}$  and  $r_{n[1-2]}$ , performed on a distance  $2D$  on either side of the wake centerline are quite similar. Once again, this is a consequence of the experimental symmetry with respect to the centerplane  $z = 0$ . For the spanwise distance of  $4D$ , the correlation coefficient  $r_{n[0-2]}$  is reduced by a factor of 2.

### 3.2. Controlled wake

In the following sections, we will present the results of experiments when a small circular control cylinder is placed in the wake. Two diameters of control cylinder will be tested, the smallest control cylinder of diameter  $1mm$  is always smaller than the mixing layer thickness that develops in the wake, since its smallest thickness which is obtained at the trailing edge of the body is  $1.25mm$  (see previous section 3.1). The other control cylinder diameter is  $3mm$ . We will show the maps of sensitivity of the wake for both control cylinders, as well as focus in detail on what happens when the control cylinder is displaced vertically across the wake at a chosen downstream distance from the main cylinder.

#### 3.2.1. Hot-wire local measurements

Figure 5(a-b) illustrates how the spectra of the velocity signals change when the control cylinders of (a)  $1mm$  and (b)  $3mm$  are displaced vertically across the wake at constant

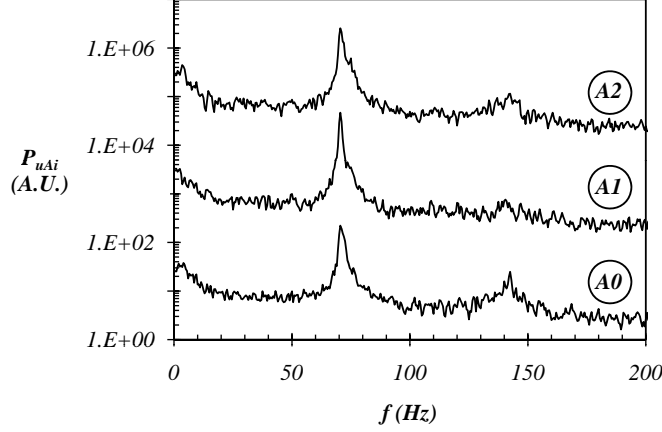


FIGURE 4. The power spectra of the velocity signals for the natural flow measured at the three spanwise locations (see figure 1b). Starting from A0, each subsequent spectrum is shifted by a decade, for visibility purposes.

$x_c = 0.4D$ . The spectra are measured by the three hot wire probes A0, A1 and A2 as depicted in figure 1(b).

If we compare the spectra between the three spanwise measurements for both sizes of the control cylinder, we can see very similar changes of both the frequency and the amplitude. We can conclude that the main effects imposed by the control cylinder are on average two-dimensional. Furthermore, the effects on the selected frequency  $f$  (where the spectrum amplitude is the largest) are symmetric with respect to the horizontal axis  $y = 0$ . Considering that the measurement points are fixed at  $y = -0.5D$ , the local measurements experiment is never symmetric with regard to the horizontal axis. Thus, the frequency symmetry  $f(y_c) = f(-y_c)$  confirms that the frequency is a global quantity, independent of where it is measured in the wake. On the other hand, the maximum amplitude of the spectra is not completely symmetric. The largest differences are observed for positions  $y_c < -0.5D$  and  $y_c > +0.5D$ . In the former case, the control cylinder is on the same side of the horizontal axis of the wake, as the hot wire probes, while in the latter they are on the opposite sides which is clearly affecting the recorded amplitude.

Now we will analyze in more detail the results for each of the control cylinder sizes. In the case of the  $1mm$  cylinder presented in figure 5(a), the frequency is reduced around  $y_c = \pm 0.6D$  for all three spanwise locations of the measurements. The amplitude, however, is different between the three measurement points and is also changing depending on the vertical position of the control cylinder. We can observe a higher amplitude when the control cylinder is in the range of  $[-0.5D, 0.5D]$ . The recorded amplitudes are lowest on the wire A0 and highest on A1. Wire A2 shows the worst peak quality.

The  $3mm$  control cylinder in figure 5(b) has a much more pronounced impact on all the properties of the spectrum throughout the range of its positions. Most notably, we can see that the frequency changes much more than in the previous case, again around  $y_c = \pm 0.5D$ . We can observe both an increase and a decrease of frequency, where the increase is the stronger effect. The amplitude of the spectrum is completely damped for several positions while it is greatly increased when the control cylinder is in the middle

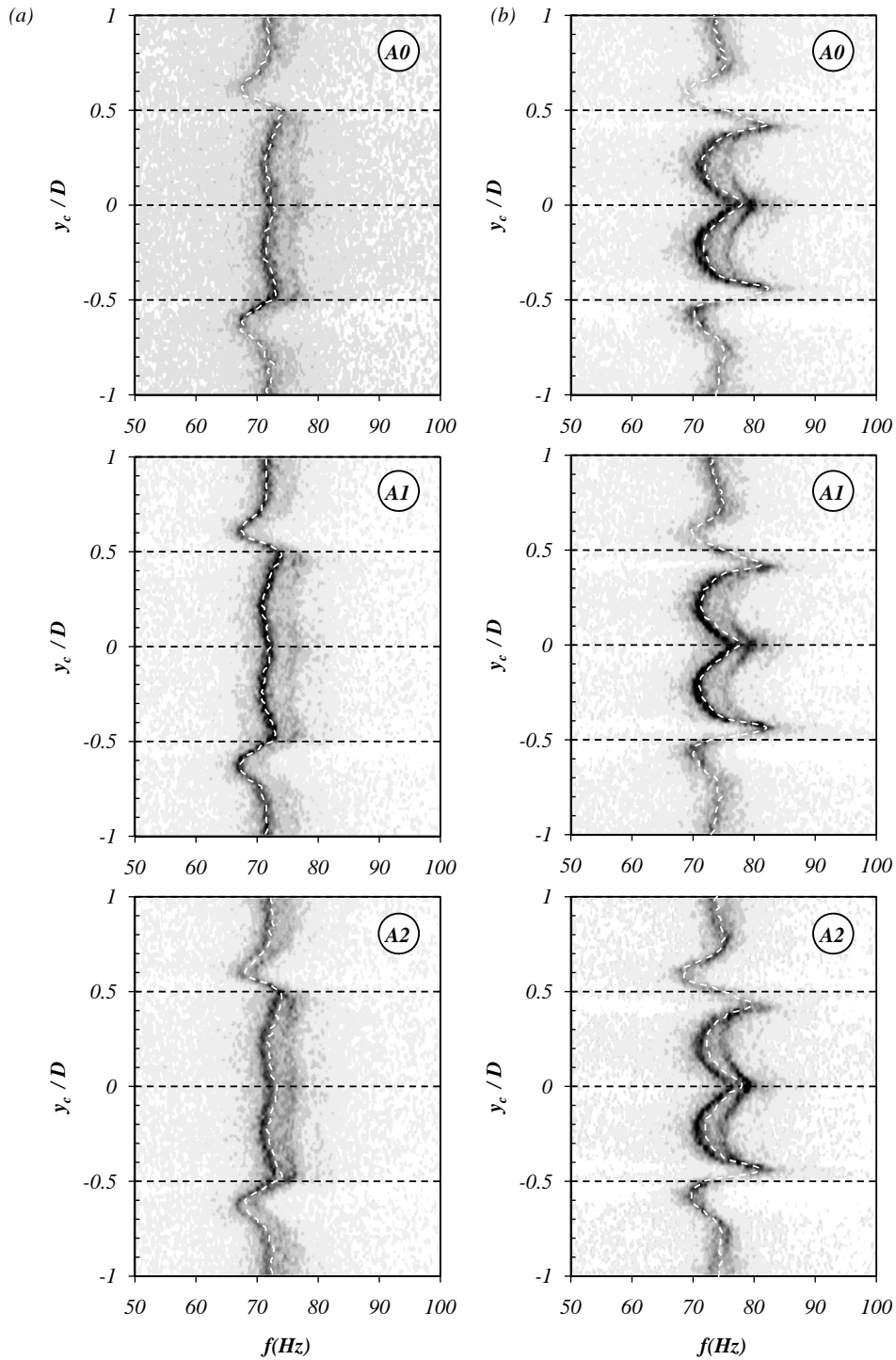


FIGURE 5. Evolution of the power spectra when the control cylinder is displaced along a vertical line at  $x_c = 0.4D$ ; (a) in the case of  $d = 1\text{mm}$ , (b) in the case of  $d = 3\text{mm}$ ; horizontal axis is the frequency, vertical axis is the vertical position of the control cylinder, and the grayscale map shows the intensity of the amplitude of the spectrum; light gray for low, and dark gray for high amplitudes.

of the wake in the range of  $[-0.4D, 0.4D]$ . Additionally, for these positions of the control cylinder, we can observe a strong modulation displayed by a second well defined energy peak. As mentioned by Parezanović & Cadot (2009b), this modulation is associated to periodic dislocations in the wake.

The actual detected frequency  $f$  (as explained in section 2.3) which is shown in figure 5 as the dashed white line is related to the energy distribution in the spectra. When we have a well defined energy peak, the detected frequency is corresponding very well as in the case of wire A1 in figure 5(a). When the spectrum is dominated by the modulation with the two energy peaks, the detected frequency is closer to the frequency of the stronger peak as can be seen for wire A2 in figure 5(b). However, regardless of the subtle differences of the energy distribution in the spectra between different hot wire probes, the detected frequencies are in good agreement between each other. If we assemble the detected global mode frequency for each position of the control cylinder, we obtain a map of the sensitivity for the global mode frequency to the presence of the control cylinder as shown in figure 6(a) and in figure 6(b) for both cylinders. The selected global mode frequency is represented as  $\tilde{f} = \frac{f-f_n}{f_n}$ . As in figure 5 we can show three maps for each control cylinder size obtained from the same three hot-wire probes. We can confirm that the detected frequency is changing in an identical fashion all along the span of the main cylinder, because there are no noticeable differences if we compare the appropriate maps between probes A0, A1 and A2. This is true for both  $1mm$  and  $3mm$  control cylinders.

The analysis of the envelope of the frequency change shows that it ranges from  $-7\%$  to  $+4.5\%$  for the  $1mm$  and  $-14\%$  to  $+20\%$  for the  $3mm$  control cylinder. For the  $3mm$  control cylinder, the increase of frequency is stronger than the decrease as was indicated by the analysis of figure 5. However, the maps give us a new piece of the puzzle which was not apparent from the analysis on only one vertical line: there are significant differences in the topology of the maps between the  $1mm$  and  $3mm$  cases. If we superimpose the natural mean recirculation bubble shape over the map (plotted with the dashed line), we can observe how in the case of  $1mm$  the effects follow the contour of the mean bubble. This is not true for the  $3mm$  case which indicates strong modifications of the mean flow. The  $3mm$  control cylinder is able to change the frequency much farther downstream than the  $1mm$ , especially in two very distinct regions adjacent to the  $y_c = \pm 0.5D$  lines. The regions of frequency reduction are smaller but the effect is doubled in the  $3mm$  case. For the  $d = 3mm$  case, we also observe a frequency increase in two regions symmetric to the  $Ox$  axis and centered at  $x_c = 0.75D$ ,  $y_c = -0.70D$  and  $x_c = 0.75D$ ,  $y_c = +0.70D$ , and a smaller third region located around  $x_c = 0.4D$ ,  $y_c = 0$ . These are not observable for the  $1mm$  case. All of these differences will be analyzed in detail using PIV measurements of the wake in section 3.2.2.

### 3.2.2. PIV global measurements

We will restrict PIV measurements to different positions of the control cylinder along a vertical line at constant  $x_c = 0.4D$  (as previously presented in figure 5). For each position, we perform a PIV acquisition and extract the mean streamwise velocity  $\bar{u}$ , mean component of vorticity in  $xOy$  plane  $\bar{\omega}_z$  and the Reynolds stresses  $\overline{v'^2}$  and  $\overline{u'v'}$ . Due to the symmetry of the experiment, confirmed by the frequency sensitivity maps, we perform PIV measurements only when the control cylinder is placed in the lower half of the wake from  $y_c = [0.08D, -0.82D]$ , in steps of  $0.02D$ . This gives us the information about 45 flows each corresponding to a different position of the control cylinder.

The study of all of these flows leads to a classification into five typical configurations. A configuration is defined from the longitudinal velocity  $\bar{u}$  seen by the control cylinder and its relative position with regard to the closest detached shear layer from the main

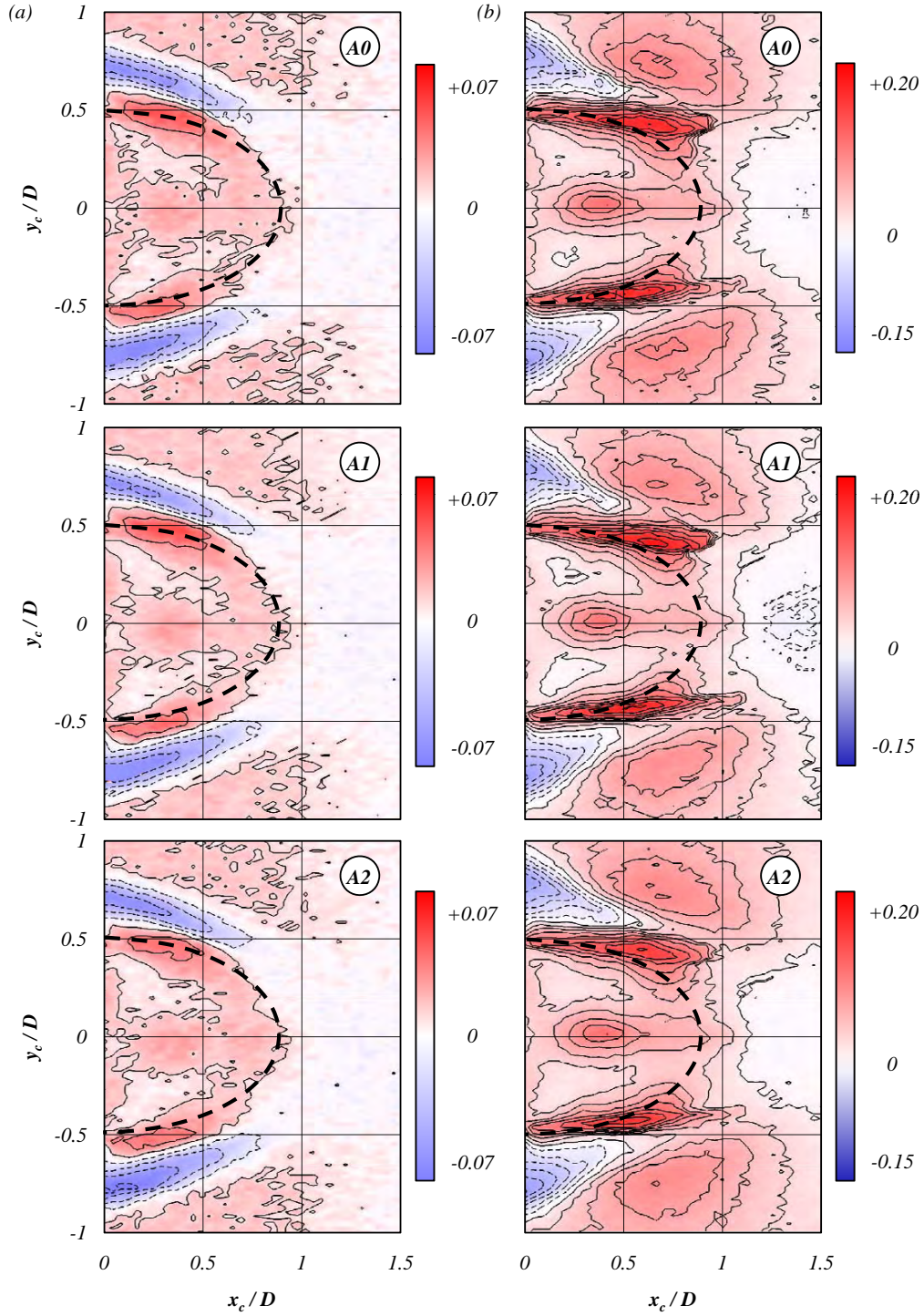


FIGURE 6. Global mode frequency sensitivity maps  $\tilde{f}(x_c, y_c)$ . The hot wire probe, from which the map is built, is indicated in the top right corner of each map. Blue color designates a decrease and red an increase in frequency compared to that of the natural frequency,  $\tilde{f} = \frac{f-f_n}{f_n}$ . Dashed line depicts the shape of the natural flow recirculation bubble. Vertical column of sensitivity maps (a) for  $d = 1\text{mm}$  control cylinder, and (b) for the case of a  $d = 3\text{mm}$  control cylinder. The isolines are in the intervals of 0.02, continuous for positive and dashed for negative values.



cylinder. The five configuration types are: *RF* for reversed flow, *IS* for inner shear, *MS* for mid-shear, *OS* for outer shear and *EF* for external flow. Typical mean fields of the longitudinal velocity  $\bar{u}$  and vorticity  $\bar{\omega}_z$  of these configurations are respectively plotted in figures 7(a-b) for  $d = 1mm$  and in figures 8(a-b) for  $d = 3mm$ .

In the *RF* configuration, the control cylinder is surrounded by a negative longitudinal mean velocity. It is located inside the isoline  $\bar{u} = 0$  in figures 7(a) and 8(a) and illustrated by the position  $y_c = 0$  of the control cylinder.

In the *IS* configuration, the control cylinder crosses the  $\bar{u} = 0$  contour line and starts to see the positive velocity of the recirculation bubble and partly the high velocity of the shear. A major ingredient of this configuration is that the totality of the shear layer detached from the main cylinder lies on one side of the control cylinder, which is an equivalent of it being reattached. This is depicted in figure 7(b) or in figure 8(b) for  $y_c = -0.4D$ . For this configuration, the control cylinder concentrates the vorticity of the primary shear. This is observable on both figures because the intermediate isoline at  $+1000$  of the controlled shear extends further downstream than the isoline at  $-1000$  from the unaffected shear.

In the *MS* configuration, the shear layer detached from the main cylinder is split by the control cylinder. This is case for positions  $y_c = -0.5D$  and  $y_c = -0.54D$  for the  $1mm$  control cylinder in figure 7(b) and for positions  $y_c = -0.42D$  and  $y_c = -0.48D$  for the  $3mm$  control cylinder in figure 8(b). One part of the shear is reattached on the control cylinder and another part is deviated between the control cylinder and the trailing edge of the main cylinder. In addition to this split, some vorticity of opposite sign is created from the control cylinder. This is best observed for the  $3mm$  control cylinder at  $y_c = -0.48D$ . This shear of opposite sign of vorticity together with the primary shear that is deviated inside the recirculating region creates a jet oriented toward the interior of recirculating region. The jet is also observable in the corresponding field of the longitudinal velocity (figure 8a,  $y_c = -0.48D$ ). The vorticity contained in the split part of the primary shear that is not deviated is much more concentrated than that of the unaffected shear. This is observed in the vorticity isolines similar as for the *IS* configuration.

In the *OS* configuration the primary shear is no longer split, but still interacts with the shear of opposite sign created by the control cylinder that is now in a region of large streamwise velocity. Due to the interaction, there is some vorticity cancellation in the controlled shear (see  $y_c = -0.68D$  in figure 7b and  $y_c = -0.62D$  in figure 8b). In case of the  $3mm$  diameter control cylinder, the recirculation region is significantly deformed, squeezed vertically and elongated horizontally as shown in figure 8(a) for  $y_c = -0.62D$ .

Finally in the *EF* configuration, the control cylinder is far enough from the primary shear to not have any direct vorticity interaction. However,  $\bar{u}$  and  $\bar{\omega}_z$  still show slight effects of the control cylinder. For the case of  $d = 3mm$ , we can observe subtle displacement of the mean bubble upwards and slight reduction of the  $\bar{\omega}_z$  in the bottom primary shear.

In the following, we study the main features of each configuration with regard to the spatial structure of Reynolds stress components  $\overline{v'^2}$  and  $\overline{u'v'}$ . They are presented in figure 9 for the  $1mm$  control cylinder and in figure 10 for the  $3mm$  control cylinder.

For the case of the  $1mm$  control cylinder some subtle changes can be observed in the *MS* configuration for which the maxima of  $\overline{v'^2}$  (figure 9a) is badly defined and its amplitude reduced. For the same configuration, we can see that the extrema of  $\overline{u'v'}$  (figure 9b) are slightly shifted downstream and their amplitudes also reduced.

We can observe in figure 10(a-b) that the  $3mm$  control cylinder makes a much bigger impact on the Reynolds stresses. We can clearly observe that the maximum of  $\overline{v'^2}$  starts

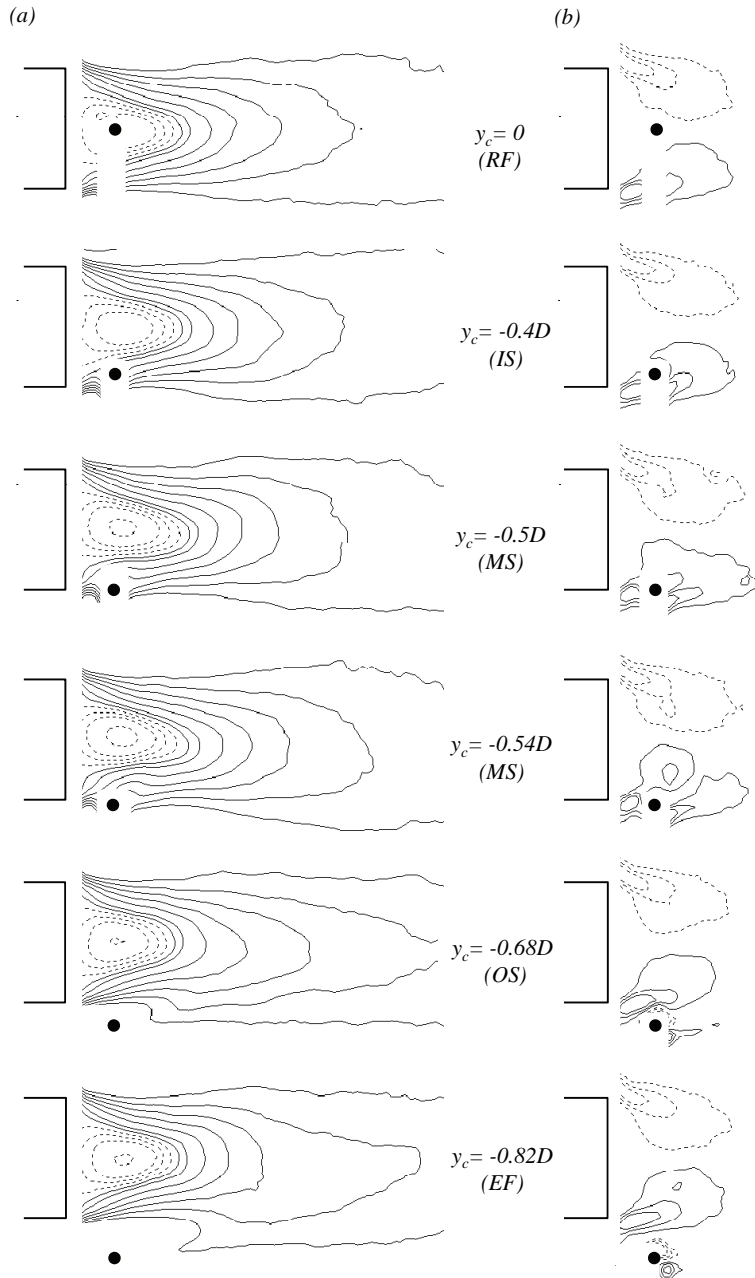


FIGURE 7. Flow for characteristic positions of the 1mm control cylinder, presented as mean streamwise velocity,  $\bar{u}$  (a) with continuous lines for positive and dashed lines for negative values, from the list  $[-3, -2, -1, -0.5, 0, 0.5, 1, 2..8]m/s$ ; and mean vorticity  $\bar{\omega}_z$  (b), where lines are at  $\pm 500, \pm 1000$  and  $\pm 1500s^{-1}$  (continuous for positive, and dashed for negative vorticity). Notation *RF*, *IS*, *MS*, *OS* and *EF* refers to configurations defined in section 3.2.2.



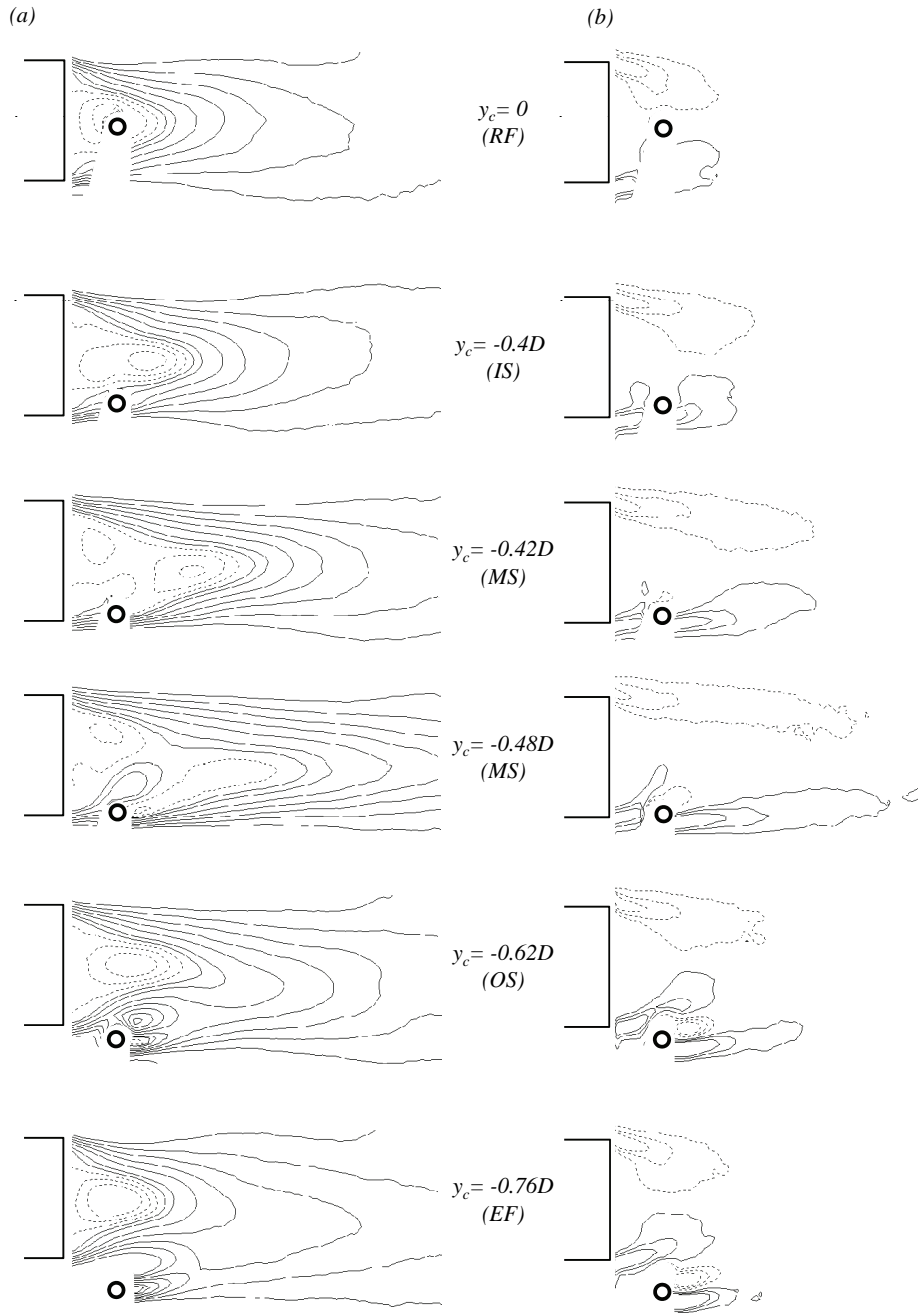


FIGURE 8. Flow for characteristic positions of the 3mm control cylinder, presented as mean streamwise velocity,  $\bar{u}$  (a) (a) with continuous lines for positive and dashed lines for negative values, from the list  $[-3, -2, -1, -0.5, 0, 0.5, 1, 2 \dots 8]m/s$ ; and mean vorticity,  $\bar{\omega}_z$  (b), isolines are at  $\pm 500, \pm 1000$  and  $\pm 1500s^{-1}$  (continuous for positive, and dashed for negative vorticity). Notation *RF*, *IS*, *MS*, *OS* and *EF* refers to configurations defined in section 3.2.2.

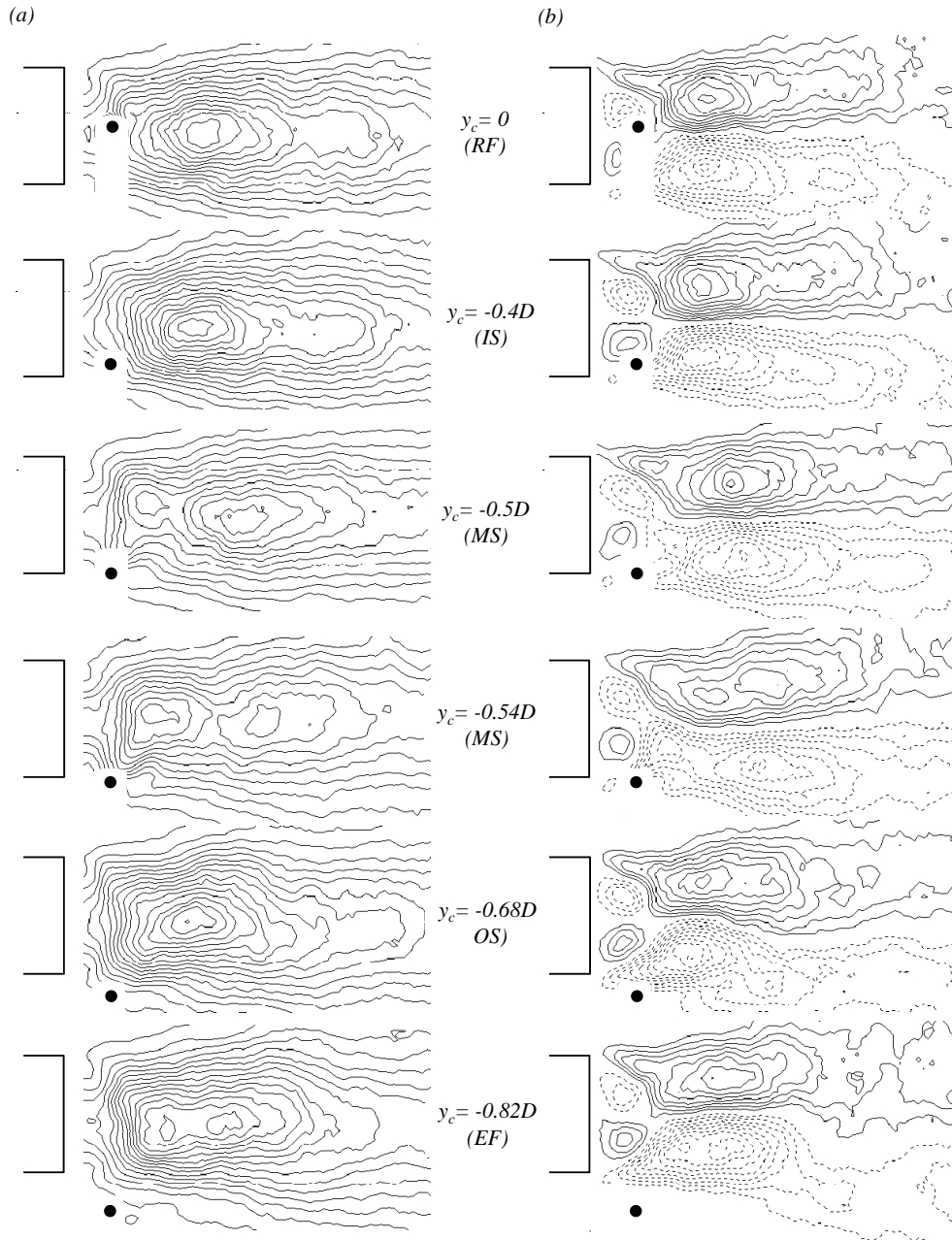


FIGURE 9. Components of the Reynolds stresses for characteristic positions of the 1mm control cylinder:  $\overline{v'^2}$ , in range of  $0(m/s)^2$  to  $15(m/s)^2$  (a), and  $\overline{u'v'}$ , in range of  $\pm 5(m/s)^2$  (b). The isolines are in the interval of  $1(m/s)^2$  (continuous lines for positive and dashed for negative values). Notation *RF*, *IS*, *MS*, *OS* and *EF* refers to configurations defined in section 3.2.2.

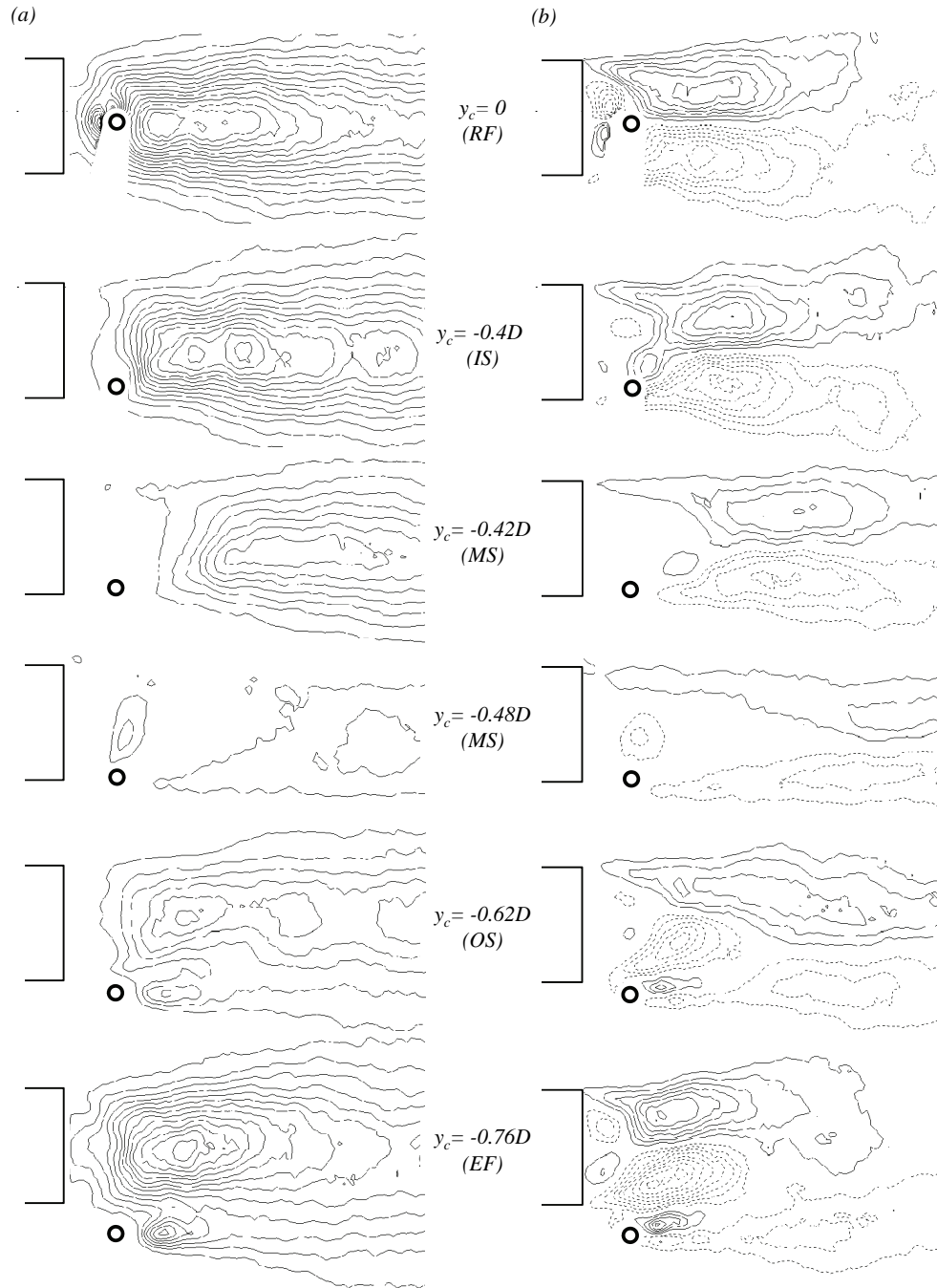


FIGURE 10. Components of the Reynolds stresses for characteristic positions of the 3mm control cylinder:  $\overline{v'^2}$ , in range of  $0(m/s)^2$  to  $15(m/s)^2$  (a), and  $\overline{u'v'}$ , in range of  $\pm 5(m/s)^2$  (b). The isolines are in the interval of  $1(m/s)^2$  (continuous lines for positive and dashed for negative values). Notation *RF*, *IS*, *MS*, *OS* and *EF* refers to configurations defined in section 3.2.2.

to shift downstream for configuration *IS* as for the extrema of  $\overline{u'v'}$ . In configuration *MS*, the extrema are shifted even further and we can observe also that the amplitude is being drastically reduced. The whole envelope of the Reynolds stress structure is completely damped and displaced downstream for the flow where the jet is most visible, at  $y_c = -0.48D$ . As the control cylinder exits the recirculating bubble for position *OS*, we can see that the locations of the extrema are gradually returning closer to the trailing edge of the main cylinder and their amplitudes are increasing. Finally, for the configuration *EF* we can observe only slight modifications to the amplitudes and locations of the extrema compared to the *RF* case. The Kármán Street of the *3mm* control cylinder is clearly seen which is not the case with the *1mm* control cylinder because of the PIV coarse graining (see section 3.1).

As we can see, some special features relevant for the global spatial structure sensitivity of the Reynolds stresses are the locations of the extrema and their amplitudes. In the case of  $\overline{v'^2}(x, y)$ , the fluctuations associated to the vortex shedding from the primary cylinder is indicated by the maximum on the center line, while it is indicated by the two extrema of opposite amplitudes symmetrically located with respect to the horizontal axis in the  $\overline{u'v'}(x, y)$  fields (see for example, *RF* configuration for  $y_c = 0$  in figure 9a-b). Their amplitudes,  $\overline{v'^2}_{Max}$ ,  $\overline{u'v'}_{Max}$ ,  $\overline{u'v'}_{Min}$  and respective abscissas  $X_{\overline{v'^2}_{Max}}$ ,  $X_{\overline{u'v'}_{Max}}$ ,  $X_{\overline{u'v'}_{Min}}$  as well as the recirculation bubble length  $L_b$  are plotted in figure 11(a-e) for the *1mm* control cylinder and in figure 12(a-e) for the *3mm* control cylinder.

For all the positions of the *1mm* control cylinder, the relative positions of the three extrema are always similar (figure 11a-b). The only significant change is the slight displacement of these positions in the *MS* configuration corresponding to a downstream shift of the spatial structure of the Reynolds stresses. It is also correlated to an increase of the mean bubble length  $L_b$  (figure 11e). Correspondingly, the amplitudes of the Reynolds stresses extrema are damped, very significantly for  $\overline{v'^2}_{Max}$  in figure 11(c) but only a hint of attenuation is visible for  $\overline{u'v'}_{Max}$  and  $\overline{u'v'}_{Min}$  in figure 11(d). The reduction of the mean bubble length  $L_b$  observed in *OS* configuration in figure 11(e) is associated with an upstream shift of the abscissa  $X_{\overline{v'^2}_{Max}}$ ,  $X_{\overline{u'v'}_{Max}}$  and  $X_{\overline{u'v'}_{Min}}$  (see figure 11 a-b). In this case, there is an upstream shift of the spatial structure of the Reynolds stresses. On the other hand, there is no clear corresponding effects to this shift in the amplitudes of the extrema in figure 11(c-d). In the case of the *3mm* control cylinder in *RF* and *IS* configurations, the abscissas of the extrema in figure 12(a-b) remain mostly unchanged indicating that the Reynolds stresses structure is conserved. In *MS* configuration, the abscissas are significantly shifted downstream and a third extremum in  $\overline{v'u'}(x, y)$  (denoted as triangles in figure 12b) with a nearly constant streamwise location is observed. The presence of this extremum is due to the shear splitting (major ingredient of the *MS* configuration) and directly related to the part entering the recirculation region. This is clearly seen in figure 10(a-b) for position  $y_c = -0.48D$  as the isolated extremum of  $\overline{v'^2}(x, y)$  and negative  $\overline{v'u'}(x, y)$  located above the control cylinder. However, the vortex shedding is associated with the two extrema symmetrically located with respect to the horizontal axis, thus having the same abscissa. In *OS* configuration a significant transition is observed around  $y_c = -0.6D$  when the shear entering the recirculating region starts to couple with the upper shear to interfere with the vortex shedding. This is displayed in figure 12(b) when the upper shear extremum (denoted by filled circles) starts to shift its streamwise location  $x/D$  back, towards the position of the extremum produced by the jet (denoted by triangles), until they are symmetrically located with respect to the horizontal axis. For *MS* and *OS* configurations, the relevant extrema associated to vortex shedding are significantly displaced downstream by almost a factor of 3. This displacement is clearly correlated to an increase of the bubble length  $L_b$  (figure 12e) and

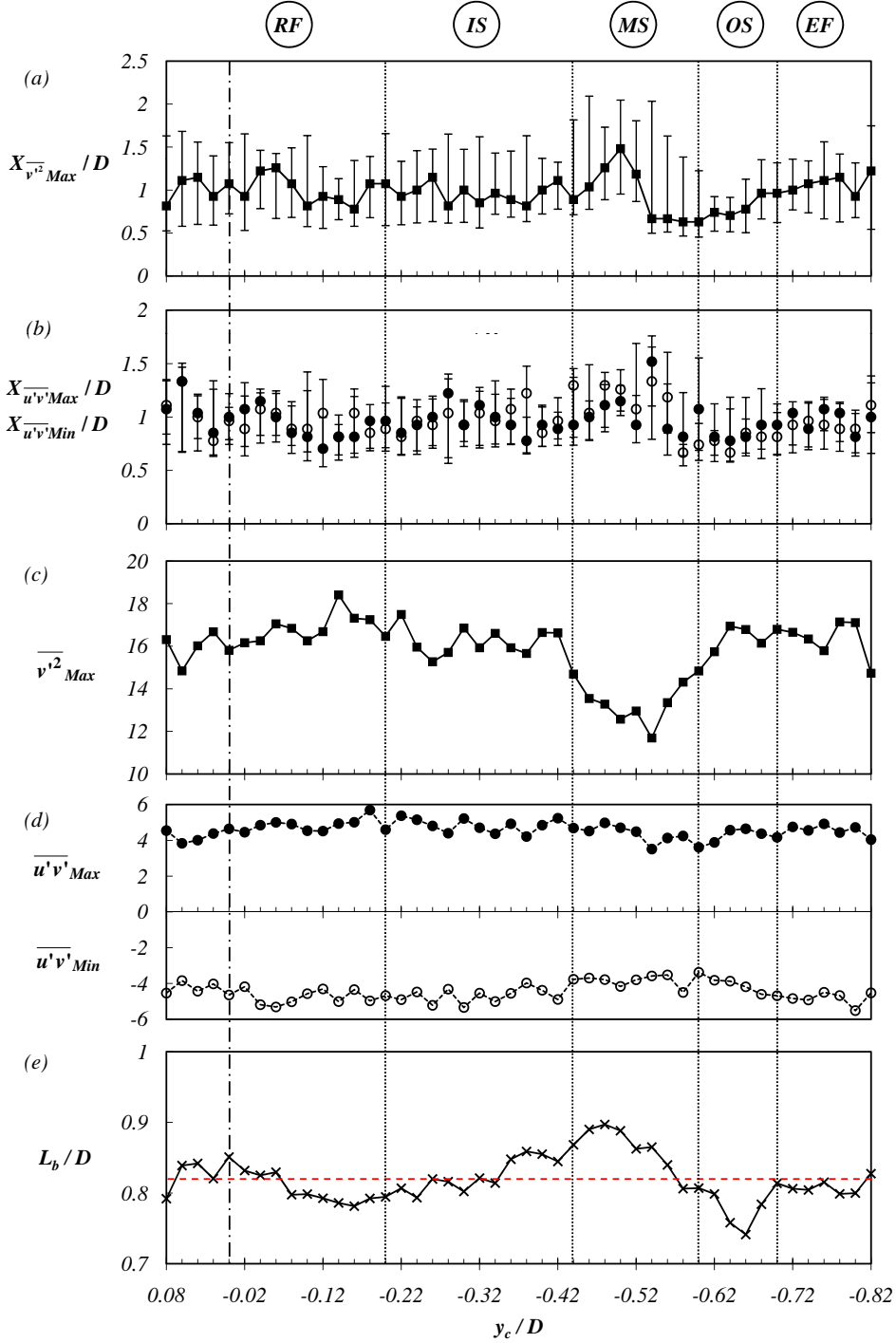


FIGURE 11. Amplitudes and streamwise locations of the extrema of Reynolds stress components  $\overline{v'^2}(x, y)$  and  $\overline{u'v'}(x, y)$  for positions of the  $1mm$  control cylinder ( $x_c = 0.4D$ ,  $-0.82D < y_c < 0.08D$ ): (a) position of the maximum of  $\overline{v'^2}$ , (b) position of the maximum (filled circles) and the minimum (empty circles) of  $\overline{u'v'}$ , (c) amplitude of the maximum of  $\overline{v'^2}$ , (d) amplitudes of the maximum (filled circles) and the minimum (empty circles) of  $\overline{u'v'}$  and (e) size of the recirculation bubble  $L_b/D$ . Notation *RF*, *IS*, *MS*, *OS* and *EF* refers to configurations defined in section 3.2.2. Error bars denote the streamwise length of the first isoline around the maximum (see figure 9).

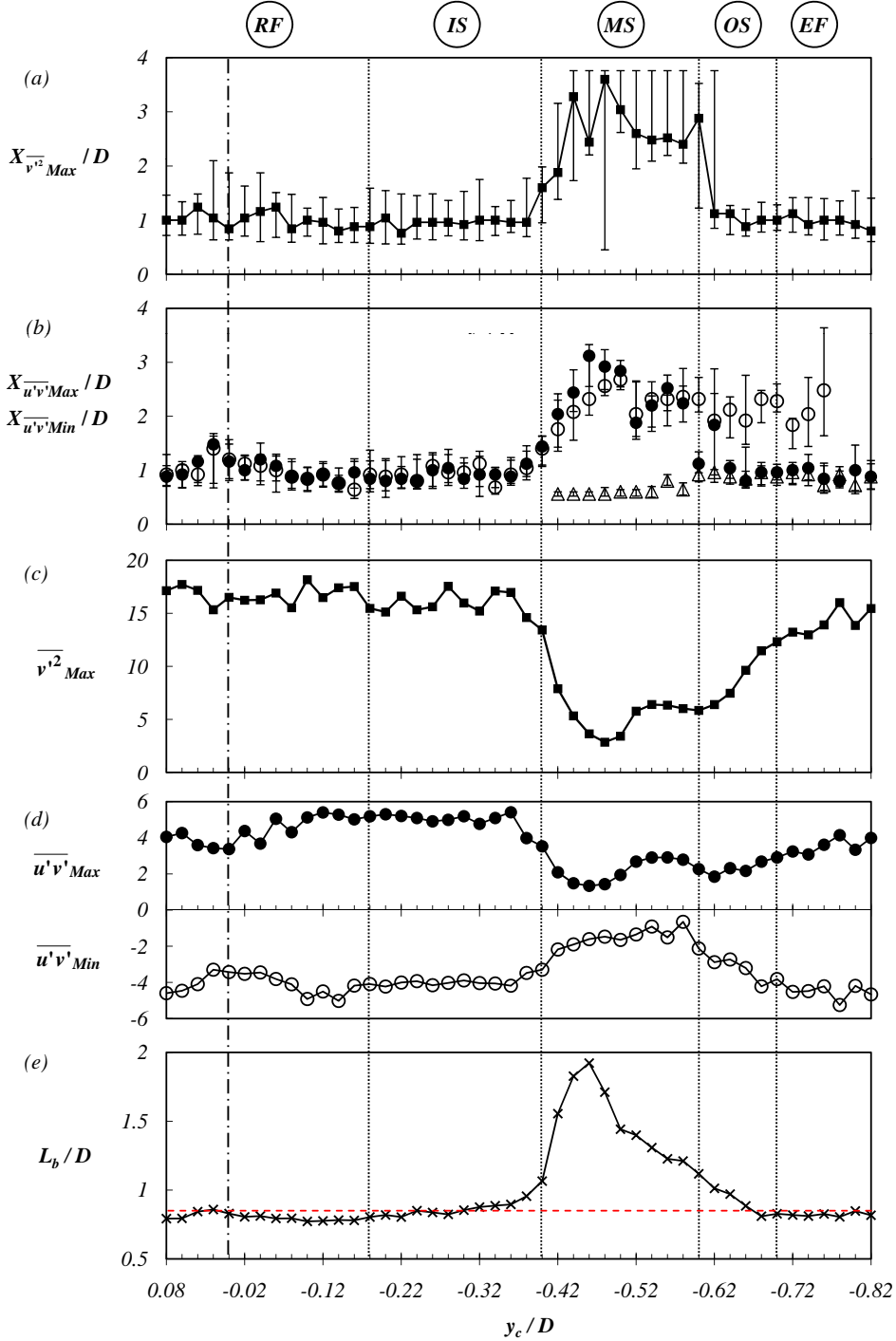


FIGURE 12. Amplitudes and streamwise locations of the extrema of Reynolds stress components  $\overline{v'^2}(x, y)$  and  $\overline{u'v'}(x, y)$  for positions of the  $3mm$  control cylinder ( $x_c = 0.4D$ ,  $-0.82D < y_c < 0.08D$ ): (a) position of the maximum of  $\overline{v'^2}$ , (b) position of the maximum (filled circles) and the minimum (empty circles) of  $\overline{u'v'}$ , (c) amplitude of the maximum of  $\overline{v'^2}$ , (d) amplitudes of the maximum (filled circles) and the minimum (empty circles) of  $\overline{u'v'}$ , the second minimum (triangles) appears in figure 10(b) for  $y_c = -0.48D$ . Size (e) of the recirculation bubble  $L_b/D$ . Notation *RF*, *IS*, *MS*, *OS* and *EF* refers to configurations defined in section 3.2.2. Error bars denote the streamwise length of the first isoline around the maximum (see figure 10).

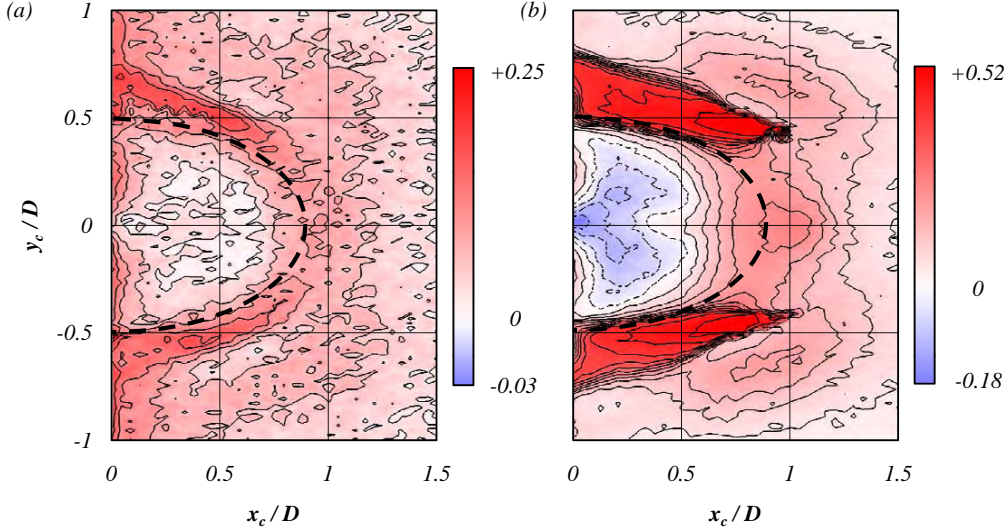


FIGURE 13. Base pressure sensitivity maps  $\tilde{C}_{pb}(x_c, y_c)$  for (a) the 1mm control cylinder with isolines interval of 0.03 and (b) the 3mm control cylinder with isolines interval of 0.05, continuous for positive and dashed for negative values. Blue color designates a decrease and red an increase in base pressure compared to that of the natural base pressure,  $\tilde{C}_{pb} = \frac{C_{pb} - C_{pbn}}{-C_{pbn}}$ . Dashed line depicts the shape of the natural flow recirculation bubble.

also associated to a strong damping of all of the extrema of the Reynolds stresses as shown in figure 12(c-d).

### 3.2.3. Base pressure measurements

The base pressure as a function of the position of the control cylinder is shown in figure 13. For both control cylinders, the major effect is to increase the base pressure. The base pressure is related to the drag in a very simple way as shown in figure 14. From these figures, it clearly appears that the control cylinders change the base pressure without influencing the pressure distribution on the frontal area of the body. Hence, the frontal contribution to the drag coefficient, denoted by  $C_0$ , is constant leading to the simple formula  $C_D = C_0 - C_{pb}$ . Comparing with global frequency sensitivity maps in figures 6, we can see that drag reduction occurring at the outer boundary of the recirculating bubble can be achieved with either frequency increase or decrease. This result excludes the role of the Strouhal number in the drag reduction mechanism. On the other hand, the base pressure modification is strongly correlated to the recirculating bubble length as can be seen for both control cylinders in figure 15 and 16. The larger the bubble length, the larger the base pressure (i.e. the lower the drag). This relationship is robust, it has also been observed for positions of the control cylinder on the horizontal axis  $x_c = 0$  (not shown here).

### 3.2.4. Spatial correlations of hot-wires local measurements

Similarly to the frequency sensitivity maps presented in the previous section, we will show how the correlation coefficient computed from Eq. 2.1 changes when the control cylinder is inserted into the wake. As a consequence of the experimental symmetry, the

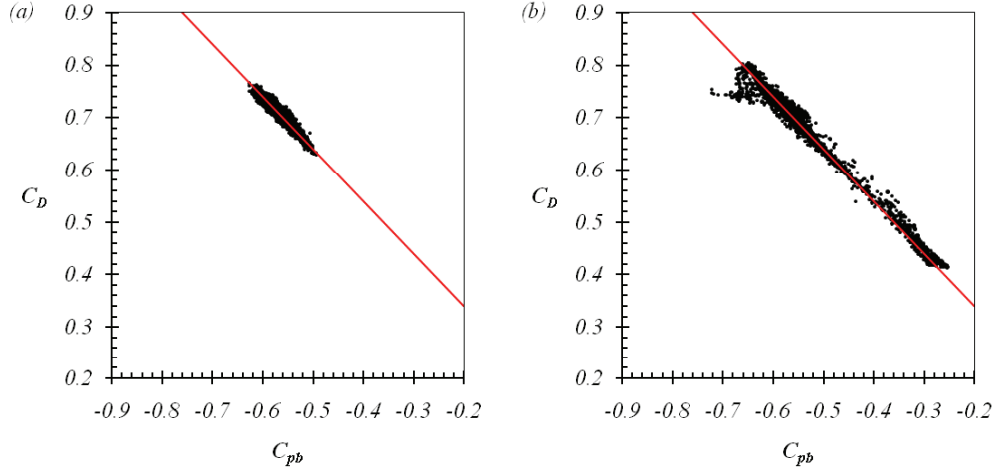


FIGURE 14. Scatter plots of the drag coefficients vs. base pressure coefficients for all the positions  $(x_c, y_c)$  of the 1mm (a) and 3mm (b) control cylinders. For both figures the straight line is  $C_D = C_0 - C_{pb}$  with  $C_0 = 0.14$ .

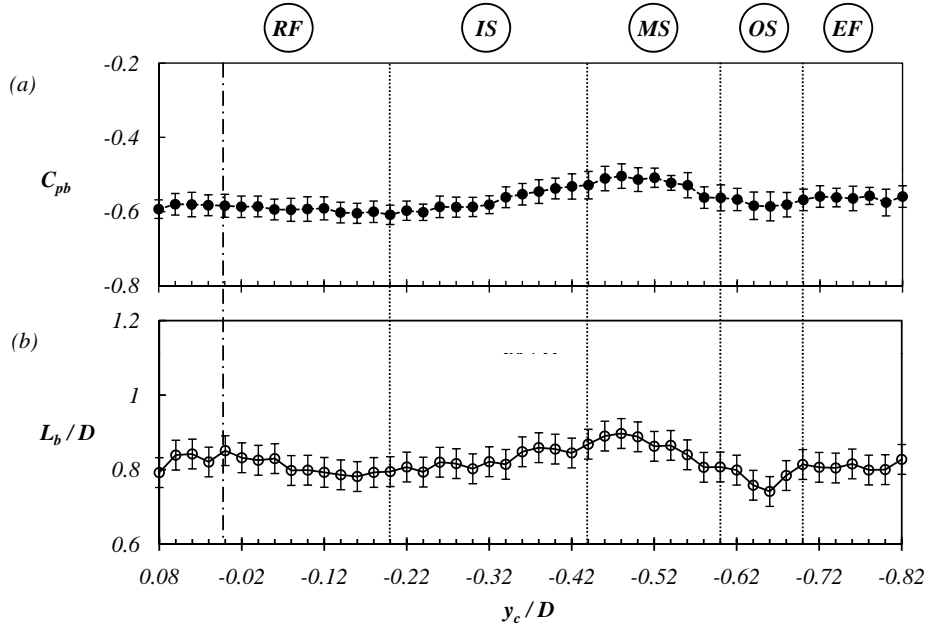


FIGURE 15. Base pressure coefficient  $C_{pb}$  (a) and recirculating bubble length  $L_b$  (b), for positions of the 1mm control cylinder ( $x_c = 0.4D$ ,  $-0.82D < y_c < 0.08D$ ). Notation *RF*, *IS*, *MS*, *OS* and *EF* refers to configurations defined in section 3.2.2. Error bars in (a) denote  $C_{pbRMS}$ ; in (b) error bars denote the uncertainty of  $L_b/D$  (see section 2.4).



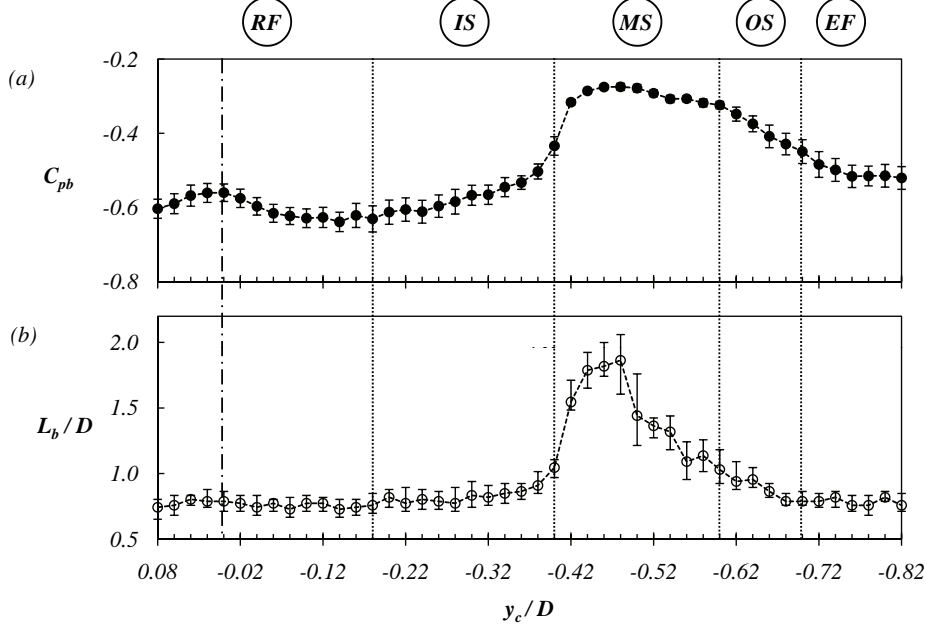


FIGURE 16. Base pressure coefficient  $C_{pb}$  (a) and recirculating bubble length  $L_b$  (b), for positions of the  $3mm$  control cylinder ( $x_c = 0.4D$ ,  $-0.82D < y_c < 0.08D$ ). Notation  $RF$ ,  $IS$ ,  $MS$ ,  $OS$  and  $EF$  refers to configurations defined in section 3.2.2. Error bars in (a) denote  $C_{pbRMS}$ ; in (b) error bars denote the uncertainty of  $L_b/D$  (see section 2.4).

sensitivity maps of  $r_{[0-1]}$  and  $r_{[1-2]}$ , both computed on a distance of  $2D$ , display the same structure and intensity. This is evidenced in the scatter plot of figure 17, by the linear relationship of slope 1 between  $r_{[0-1]}$  and  $r_{[1-2]}$ . The sensitivity map of  $r_{[0-2]}$  which is computed on a distance of  $4D$ , is identical to the others in structure but its intensity is reduced by a factor of 2 because of their linear relationships of slope  $1/2$  (see figure 17). These observations are identical for both control cylinders. The spanwise correlation can then be described from only one correlation coefficient that will be chosen as  $r_{[0-1]}$  and is shown in figure 18(a) for the  $1mm$  control cylinder. In this case, correlation coefficient changes are in the range of  $0 < r < +0.39$  and we can conclude that the presence of the control cylinder can significantly improve the correlation as well as it can reduce it. The correlation is improved when the control cylinder is inside the recirculation bubble or on its boundary. When the control cylinder is outside, either above or below the wake, the correlation is reduced. The effects of the  $3mm$  control cylinder on the correlation coefficient can be seen in figure 18(b). The changes are in the range of  $-0.08 < r < +0.506$ . As for the  $1mm$  control cylinder, the correlation is always increased when the control cylinder is inside the bubble. The main difference is observed at boundary of the mean recirculation bubble, where there are two regions of strong reduction of correlation. These regions are spatially very similar to regions of increased base pressure coefficient (see figure 13). The reduction sometimes reaches negative values in the upper region.

For both sizes of the control cylinder, the sensitivity maps of  $r$  show some sort of symmetry with respect to  $Ox$  axis. We remind the reader that due to position of the velocity measurements (see section 2.1), that is not on the horizontal axis of the experiment, there

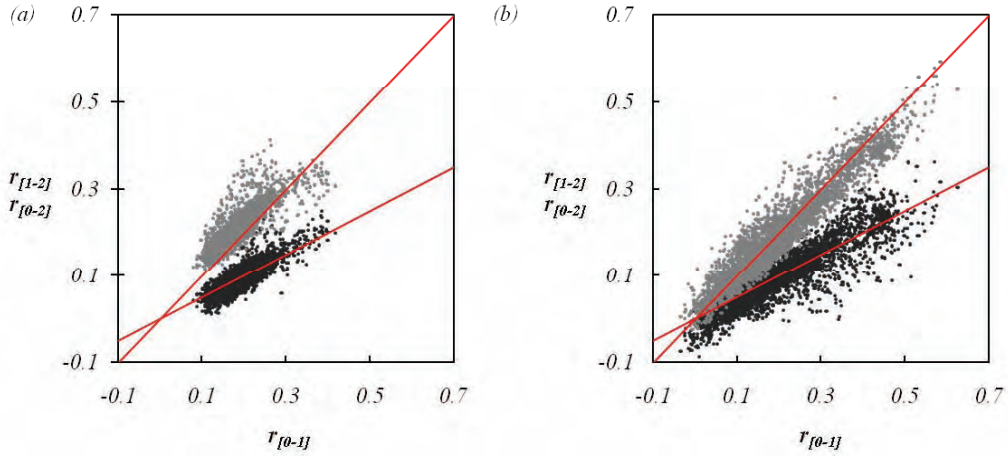


FIGURE 17. Scatter plot of correlation coefficients  $r_{[0-1]}$  vs.  $r_{[1-2]}$  (light points), and  $r_{[0-1]}$  vs.  $r_{[0-2]}$  (dark points), for (a) 1mm and (b) 3mm control cylinder. Lines correspond to linear relationship slope of 1 and 1/2.

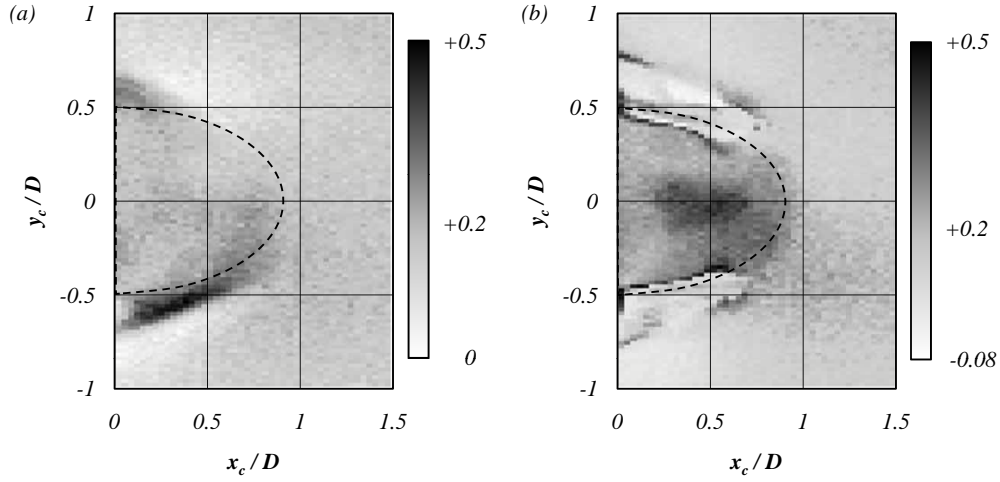


FIGURE 18. Sensitivity maps of the spanwise spatial correlation coefficient  $r(x_c, y_c)$ ; for (a)  $d = 1mm$ , and (b)  $d = 3mm$ . Dashed line depicts the shape and size of the mean recirculation bubble for the natural flow.

is no symmetry that imposes identical measurements for two symmetric positions  $\pm y_c$  of the control cylinder. Then the pseudo-symmetry in figure 18(a) and (b) indicates that even if the measurement of the correlation is local, it remains influenced by the global properties of the wake.

## 4. Discussion

Based on the presented results in the previous chapter, we will now discuss and propose possible mechanisms that are responsible for the global mode frequency selection, global mode amplitude and spatial structure, mean wake modifications and base pressure changes.

### 4.1. Global frequency selection

As already mentioned in Parezanović & Cadot (2009a), the global frequency is related to the vorticity distribution in the shear layers detached from the main cylinder which is influenced by the vorticity created from the control cylinder. Two mechanisms were observed, one due to a vorticity feedback in the *RF* configuration and the other due to a direct interaction corresponding here to the *IS*, *MS* and *OS* configuration. In order to elucidate on these relationships, the vertical profiles of  $\bar{\omega}_z(y)$  just downstream from the control cylinder, at  $x/D = 0.44$  is extracted for all the positions of the control cylinder  $y_c$ . The obtained sequence  $\bar{\omega}_z(y, x = 0.44D, y_c)$  is plotted respectively in figure 19(a) for the *1mm* cylinder and figure 20(a) for the *3mm* cylinder. The global frequency changes  $\tilde{f}(y_c)$  is plotted in figure 19(b) for the *1mm* control cylinder and figure 20(b) for the *3mm* control cylinder. From the analysis of the extrema of the Reynolds stresses structure in section 4.2, it is sometimes possible to deduce which interacting shear layers are responsible for the vortex shedding (i.e. the global mode). They are marked by blue and red colored lines in the figure 19(a) and figure 20(a). The lines are computed as the vorticity barycenter of the corresponding vorticity distribution.

These figures emphasize the role of the vorticity distribution in the shears (Gerrard 1966) and their separating distance (Roshko 1954) in the selection of the global mode frequency. By inserting the control cylinder for a flow configuration *IS*, we observe that the vorticity in the affected shear is more concentrated and consequently, the shear is becoming thinner. This occurs as the cylinder progresses toward the *MS* pattern, for both control cylinder sizes. It is worth noticing that the separating distance of the shears (marked by the colored lines) remains unchanged. The thinning of the controlled shear means that the time needed for interaction of two shears to complete a vortex shedding is shorter (Gerrard 1966), which is consistent with the corresponding frequency increase (figure 19-20) in the *IS* configurations. At some point the control cylinder starts to move the controlled shear linearly away from the center of the wake. As a result, the increase of the separating distance will counter effect the vorticity concentration. The balance between these two effects will lead to saturation and then to a decrease of the selected frequency as observed in flow configuration *MS*. In the case of the *3mm* control cylinder the separating distance is magnified by the presence of the jet (see section 3.2.2) that pushes away the uncontrolled shear (see figure 20a). In the *OS* configuration for the *1mm* control cylinder, the frequency is still very low because the vorticity in the controlled shear is weakened by the vorticity of opposite sign produced by the control cylinder. The mechanism of vorticity distribution is then again dominant as in *IS* configuration but in an inverse manner; vorticity is reduced and the shear becomes thicker. For configuration *EF*, the influence of the *1mm* control cylinder becomes negligible and frequency gradually increases, to obtain its natural value. In the case of the *3mm* cylinder, the frequency reaches a minimum when the separating distance is the largest at  $y_c = -0.58D$ . However, the global vorticity dynamics in the *OS* configuration is confounded by the fact that there are four different layers of vorticity which are interacting. Because of this complex interaction, the *OS* region serves as a transition region between the frequency minimum in *MS* and the increased frequency in the *EF* configuration. It is then impossible to identify which shears are interacting. This is why the barycenter lines in the *OS* region

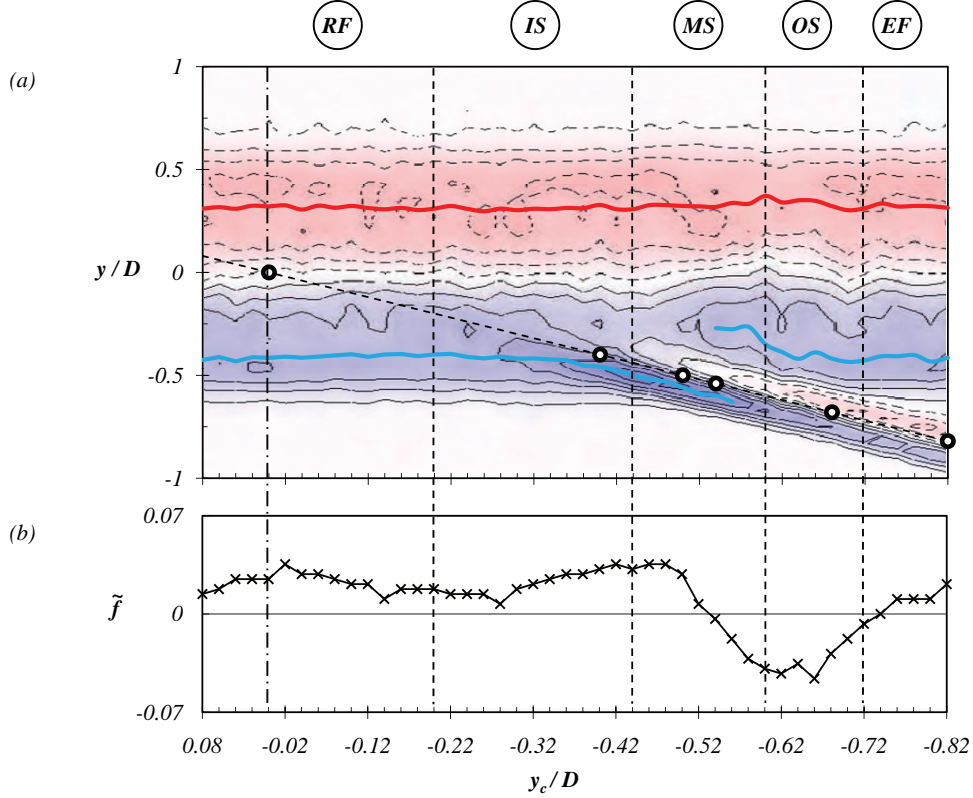


FIGURE 19. (a) Mean vorticity sequence  $\bar{\omega}_z(y, x = 0.44D, y_c)$ , for the 1mm control cylinder, showing the vertical vorticity distribution across the wake downstream of the control cylinder ( $x_c = 0.4D, y_c$ ). The contours of vorticity are the same as in figure 7(b). The dashed line denotes the path of the control cylinder across the wake, and circles represent the positions of the control cylinder presented in figure 7 and figure 9. Diagram (b) shows frequency  $\tilde{f}$  of the global mode. Notation  $RF$ ,  $IS$ ,  $MS$ ,  $OS$  and  $EF$  refers to configurations defined in section 3.2.2.

are overlapping and are denoted by dashed lines. The size of the 3mm control cylinder is sufficient to maintain a strong modification of the wake in  $EF$  configuration, which results in separating distance smaller than in the natural case, while vorticity remains unchanged. Hence, the frequency is higher than natural in the  $EF$  pattern.

#### 4.2. Global mode structure and drag reduction

The spatial structure of the global mode should be extracted from the coherent part of the Reynolds stress that is synchronized at the global frequency. For cylinders, and in the near wake, the main contribution of the fluctuations to energy in the spectral domain is localized around the synchronized frequency of the global mode (see for example figure 4). Hence, our measurements of Reynolds stresses displayed in figure 9 and figure 10 are also relevant to the structure of the global mode. The main effect of the control cylinder is to displace downstream the extrema of the Reynolds shear stresses that are associated to the vortex shedding. This effect is accompanied by amplitude damping. It seems then natural to conclude that as for the Reynolds stresses, the global mode struc-

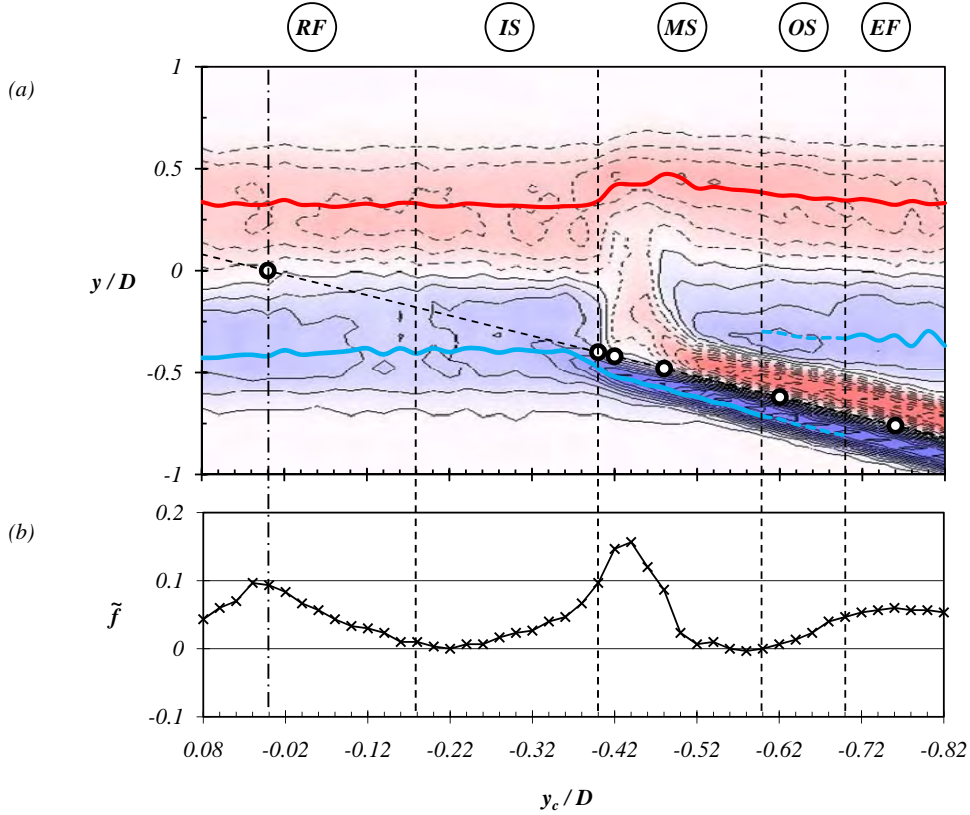


FIGURE 20. (a) Mean vorticity sequence  $\bar{\omega}_z(y, x = 0.44D, y_c)$ , for the 3mm control cylinder, showing the vertical vorticity distribution across the wake downstream of the control cylinder ( $x_c = 0.44D, y_c$ ). The contours of vorticity are the same as in figure 8(b). The dashed line denotes the path of the control cylinder across the wake, and circles represent the positions of the control cylinder presented in figure 8 and figure 10. Diagram (b) shows frequency  $\tilde{f}$  of the global mode. Notation *RF*, *IS*, *MS*, *OS* and *EF* refers to configurations defined in section 3.2.2.

ture is displaced downstream together with the strong damping. This has already been observed in context of forced wake (Thiria *et al.* 2006; Thiria & Wesfreid 2007) near the threshold of instability at low  $Re$ . Similarly as in that study, we also find the maximum amplitude of the global mode to be roughly inversely proportional to its downstream position (figure 21). This behavior was also observed for natural wake (Goujon-Durand *et al.* 1994; Zielinska & Wesfreid 1995; Couairon & Chomaz 1999) near the threshold of the instability around  $Re = 50$ . It is interesting to find the same feature at much higher Reynolds numbers. The sensitivity of the global mode position to the control cylinder position may be interpreted with the Gerrard's model valid at large Reynolds number for the size of the formation region (Gerrard 1966). Briefly, the formation region is bounded by the detached shears from the trailing edges and the eddies roll-up. From the physical Gerrard's model, the size of the formation region results from an equilibrium of the entrainment of the detached shear layers and replenishment of fluid into the recirculation region. Any changes in these fluxes due to the presence of the control cylinder will lead to a new equilibrium with a different size of the formation region. If the controlled shear

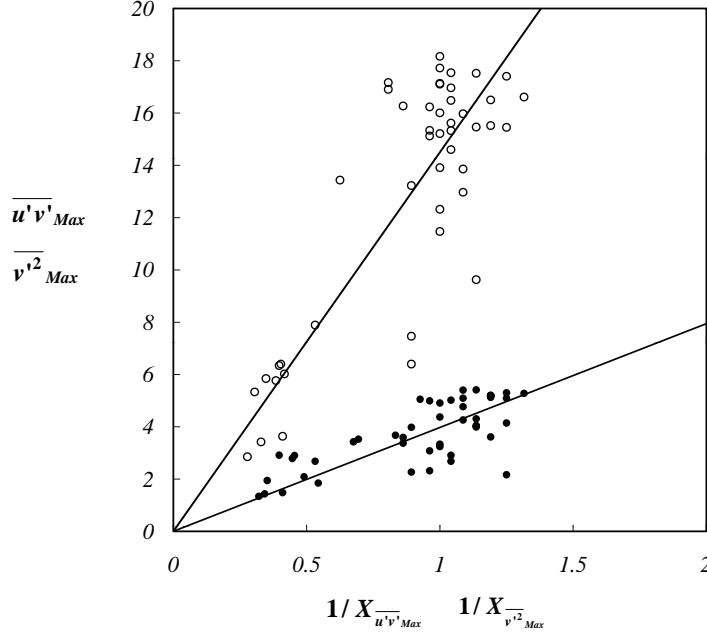


FIGURE 21. Amplitude of  $\overline{v'^2_{Max}}$  (empty circles) and  $\overline{u'v'_{Max}}$  (filled circles) versus the inverse of their respective locations for the  $d = 3mm$  control cylinder at  $x_c = 0.4D$  and  $0.08D > y_c > -0.82D$ . Straight lines are linear best fits.

gets more turbulent, then its entrainment will be increased which will reduce the formation region size. This occurs when the control cylinder approaches sufficiently close to the primary shear from outside of the recirculation region. In this case, the control cylinder is in a high velocity region and has his own unsteady wake which enhances the turbulence in the primary shear. This situation is consistent with the  $1mm$  control cylinder in the  $OS$  configuration, in which the vorticity in the controlled shear is partially canceled (figure 7b), the global mode structure shifted upstream (figure 9a-b) and the mean recirculation region length decreased. On the contrary, if the control cylinder concentrates the vorticity in the controlled shear, entrainment will be decreased and consequently the formation length increased. This effect is common for the  $IS$  configuration of the flow, for both  $1mm$  and  $3mm$  control cylinders (figure 7b and figure 8b) for which the global mode structure is shifted downstream (figure 9a-b and figure 10a-b) and the mean recirculation region length increased. A third mechanism that is responsible for the largest formation size increase, involves a direct injection of momentum in the formation region. This is clearly observable for the  $3mm$  control cylinder in configuration  $MS$  (figure 8a), in which the global mode structure is the furthest from the main cylinder (figure 10a-b), and the mean recirculation region length the largest.

From our interpretation, the sensitivity of the global mode streamwise location is a direct consequence of the modification of the size of the formation region as described above due to the presence of the control cylinder. The question that remains is about the relationship between the global mode position and global mode amplitude. Our idea is based on the role that the pressure gradients may play in the intensity of the eddies roll-

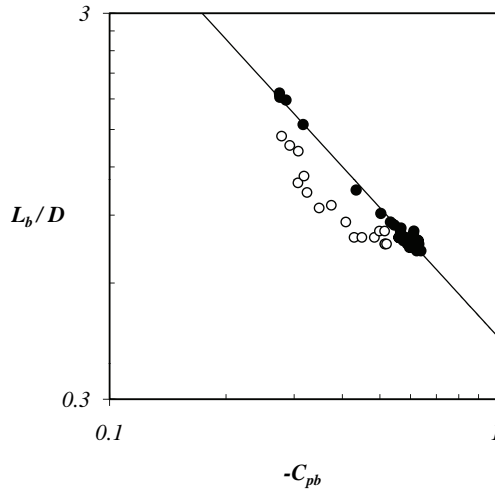


FIGURE 22. Base pressure coefficient  $C_{pb}$  as a function of the bubble recirculation length  $L_b$  for positions of the  $3mm$  control cylinder at  $x_c = 0.4D$  and  $y_c$  within the range  $0.08D > y_c > -0.48D$  (filled circles) and within the range  $-0.82D > y_c > -0.48D$  (empty circles). Straight line is a best fit with power law exponent of  $n=-1.09$ , for data denoted by filled circles only.

up. In previous papers Thiria *et al.* (2009) and Parezanović & Cadot (2009a), we have shown that the base pressure is increased each time the global mode is pushed further downstream for the  $3mm$  control cylinder. The present experiment confirms this result for the smaller  $1mm$  control cylinder. If we assume that the formation region size is the key parameter, its increase in length can create a base pressure increase (and then weaker pressure gradients), simply because a longer formation region will lead to less curvatures of the detached streamlines after the trailing edges. This is consistent with the strong correlation between the bubble length and the base pressure coefficient (see figure 15-16) and would explain the drag reduction mechanism. As a consequence, an increase of the formation region length leads the eddies to roll-up in a region of weaker pressure gradient which might explain the damping of the global mode each time it is displaced downstream. The argument that less curvature of the detached streamlines leads to higher base pressure is a feature of cavity models, based on steady potential flow theory with a closure model of the separated streamline (Wu 1972). Whatever the closure model used, it is found that for a given bluff body the relationship between base pressure and bubble length exhibits a power law  $L_b/D \propto (-C_{pb})^n$ , with  $n < 0$  depending on the model (Franc & Michel 2005). This relationship for the  $3mm$  is deduced from the figure 16 and shown in figure 22. Two tendencies are found following that the control cylinder is inside the recirculation bubble ( $y_c > -0.48$ , filled circles) or outside ( $y_c < -0.48$ , empty circles). We may find a power law dependency especially when the control cylinder is inside the recirculating bubble.

#### 4.3. Effect on the 3D properties of the wake

The three dimensional properties of the wake have been investigated with spanwise spatial correlation. The spatial correlation is increased for all the positions of the control cylinder inside the recirculating region comprising *RF* and *IS* configurations. It is decreased

when the control cylinder is in the *OS* and *EF* configurations. In the case of the *MS* configuration, it depends on the size of the control cylinder, the correlation is increased for the *1mm* control and decreased for the *3mm* control. At large Reynolds number,  $Re > 5000$ , the 3D structure of the wake of a cylinder is dominated by random-positioned vortex dislocations (Norberg 2001) causing a strong decrease in the lift fluctuations and contribute to the width of the peak at the Strouhal frequency (Prasad & Williamson 1997). It is known that these effects are correlated to the laminar to turbulent transition in the shear layers (Bloor 1964; Norberg 2001). For the *3mm* control, the clear modulation in the *RF* and also in *IS* configurations along the span indicates periodic dislocations appearances in the wake Parezanović & Cadot (2009b). This organization can be ascribed to an improvement of the feedback effect involved in the global mode synchronization and may contribute to the spanwise correlation increase. In addition, for *IS* configuration, the concentration of the controlled shear can be viewed as a relaminarization of the shear whose consequence will be to improve the spanwise correlation. Similarly, for the *OS* and *EF* configurations, the controlled shear is weaker and forced by the Kármán vortex street of the control cylinder which can be viewed as a turbulence enhancement in the shear and thus, a reduction of the spanwise correlation.

## 5. Conclusion

The objective of this paper is to elucidate on the changes in global properties when a small circular control cylinder is placed in the wake of the main bluff cylinder. The idea is to construct a sensitivity analysis of the global dynamics of a turbulent wake. The experiments involved two different sizes of the control cylinder, one is bigger than the thickness of the detached shears and the other one smaller. From the results, we have proposed a mechanism based on the efficiency of the control cylinder to change the size of the formation region. The physical mechanism explains the observed modifications of the spatial structure of the global mode and its amplitude as well as the global frequency selection and the drag reduction. The main changes in the global mode frequency are interpreted in terms of shear diffusion and separating distance between the shears participating to the global mode. The global mode spatial structure is closely related to the base pressure (ie. the drag), through the formation length.

Figure 23 summarizes the variety of effects of the control cylinders on the global dynamics of the detached shear layers:

- In the inner shear configuration, the control cylinder feeds the controlled shear with same vorticity sign, making it thinner. Reduced entrainment demands, mean that the formation region will increase its size to regain a new equilibrium.
- In the middle shear configuration the controlled shear splits, the part of it that is deviated inside the formation region is canceled by the shear of opposite sign created by the *1mm* control cylinder while it forms a jet in the case of the *3mm* control cylinder. As the result the jet inflates the formation region.
- For the *1mm* control cylinder, in the outer shear configuration, the shear of the control cylinder cancels partially the vorticity in the controlled shear, making it thicker and more turbulent. Increased entrainment demands, mean that the formation region will decrease its size to regain a new equilibrium. For the *3mm* there is no vorticity cancellation, which leads to a complex interaction between the controlled shear and the two shears of the control cylinder.
- The external flow configuration shows nearly no impact of the *1mm* control cylinder, and the formation region is close to natural value, however, *3mm* control cylinder is large enough to create a blockage effect that squeezes the formation region vertically.



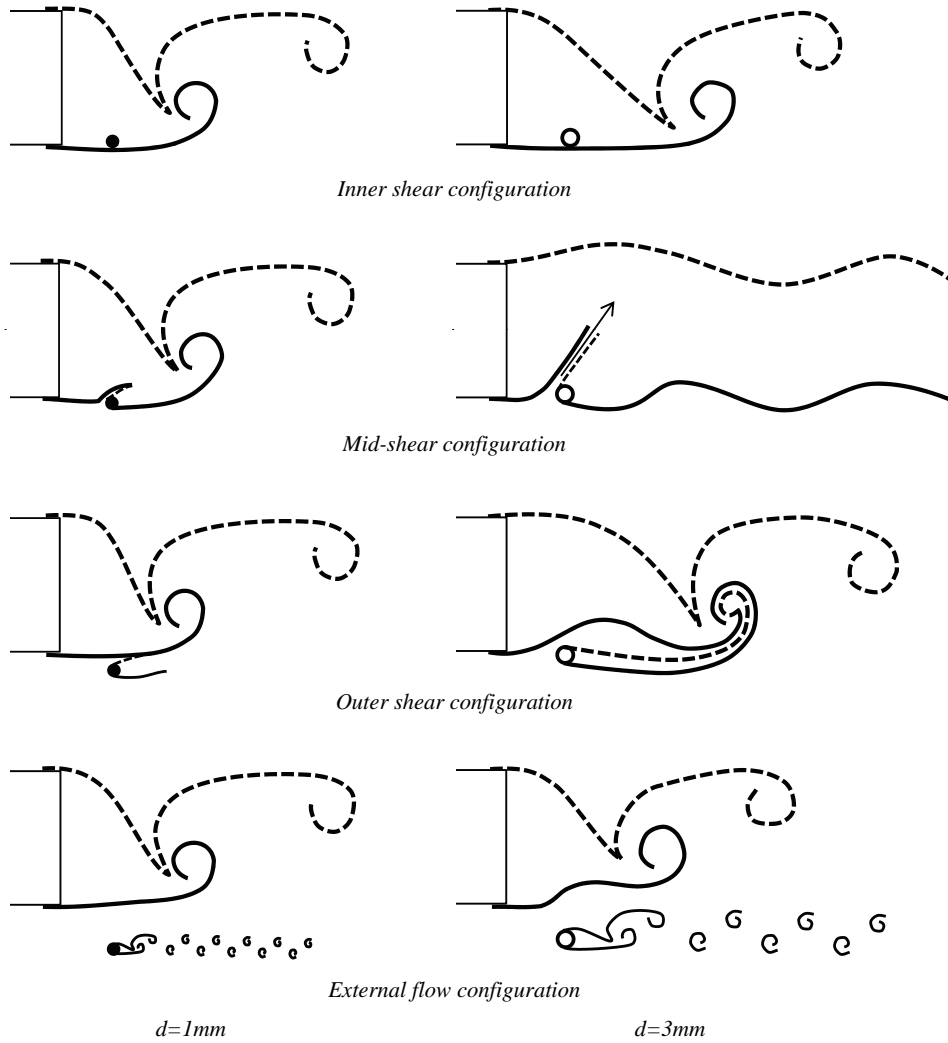


FIGURE 23. Schematic representation of characteristic wake flow patterns, observed and classified in this study.

Further experiment (Parezanović 2011) performed with a 0.1mm control cylinder have shown the same structural sensitivity as the 1mm control cylinder but with amplitudes just distinguishable from the background noise. We therefore believe that our sensitivity maps of the  $d = 1mm$  cylinder which imply only weak mean flow modifications are good candidates to be compared to future theoretical results of the structural sensitivity analysis of a turbulent wake. For this purpose we performed a complete sensitivity maps (see appendix A) of base pressure and global frequency around the bluff body which also implies boundary layer control. It would be an interesting challenge for theoreticians to recover these maps.

The authors would like to thank Prof. Patrick Huerre for his critical reading of the manuscript and his continuous interest and support of our work. We are also grateful to J. R. Wrightson and R. Monchaux for their contributions to the manuscript, and M. Grandemange for his help with the experimental work. This work was supported by the ANR project no. 06-BLAN-0363-01 "HighSpeedPIV".

## **Appendix A. Extended sensitivity maps**

The sensitivity of global properties around the main bluff cylinder is investigated with a 1mm control cylinder. The maps of the global frequency in figure 24(a) and base pressure in figure 24(b) are obtained from three different experiments to cover the entire region. The first part, which is the focus of the main article, is covering the wake area in the range  $0 < x_c/D < 1.8$  with a resolution of the control cylinder displacement of  $\Delta x_c \times \Delta y_c = 1mm \times 0.5mm$ . The second part covers the region above the flat portion of the main cylinder in the range  $-1.5 < x_c/D < 0$  with the same resolution as above. The third part covers the area in front of the semi-circular part of the main cylinder; in the range  $-2.2 < x_c/D < -1.5$ . For this area the control cylinder displacement resolution is increased to  $0.5mm \times 0.5mm$  in order to precisely follow the wall curvature. The total duration of these experiments to produce this map was 87 hours.

Figure 24(c) shows the streamlines of the natural flow as a case of reference for the mean boundary layer/shear layer locations and geometry. When the sensitivity of the wake ( $x_c > 0$ ) is investigated, the control cylinder changes neither the detachment points of the shear layers nor influence significantly the boundary layer development along the body. On the contrary, upstream of the detachment ( $x_c < 0$ ), the small 1mm control cylinder can impose strong modifications to the history of the boundary layer. The region ( $x_c > 0$ ) being thoroughly discussed in the article, we will here only comment on most prominent features of the sensitivity map for  $x_c < 0$ .

A reduction of the global frequency is clearly visible. This effect can be attributed to the vorticity cancellation mechanism (see section 4.1) since the control cylinder is just above the boundary layer. The effect of the sensitivity of the small separated region near the wall at  $-1.5 < x_c/D < -0.5$  is observable on both the base pressure and global frequency. The large base pressure increase near the wall at  $-1.5 < x_c/D < -0.5$  indicates that a thinner shear (having small entrainment velocity) initiates the wake compared to that of the natural flow (see section 4.2). This can be achieved because the control cylinder placed in a favorable pressure gradient near the wall at  $-1.5 < x_c/D < -0.5$  will provoke turbulent transition in the boundary layer and certainly suppresses the detachment at  $x_c = -1.5D$ . As a result, a thinner turbulent boundary layer should be observed at  $x_c = 0$ . A large decrease of the base pressure (blue region in figure 24b) is observed in the reattachment region of the small separated region. It indicates that a thicker shear (having large entrainment velocity) initiates the wake (see section 4.2). This can be achieved because the control cylinder placed in or after the reattachment region creates an adverse pressure gradient that is able to either increase the shear thickness or provoke early separation. The experimental verification of these assumptions is needed and the necessary work would go far beyond the scope of this appendix.

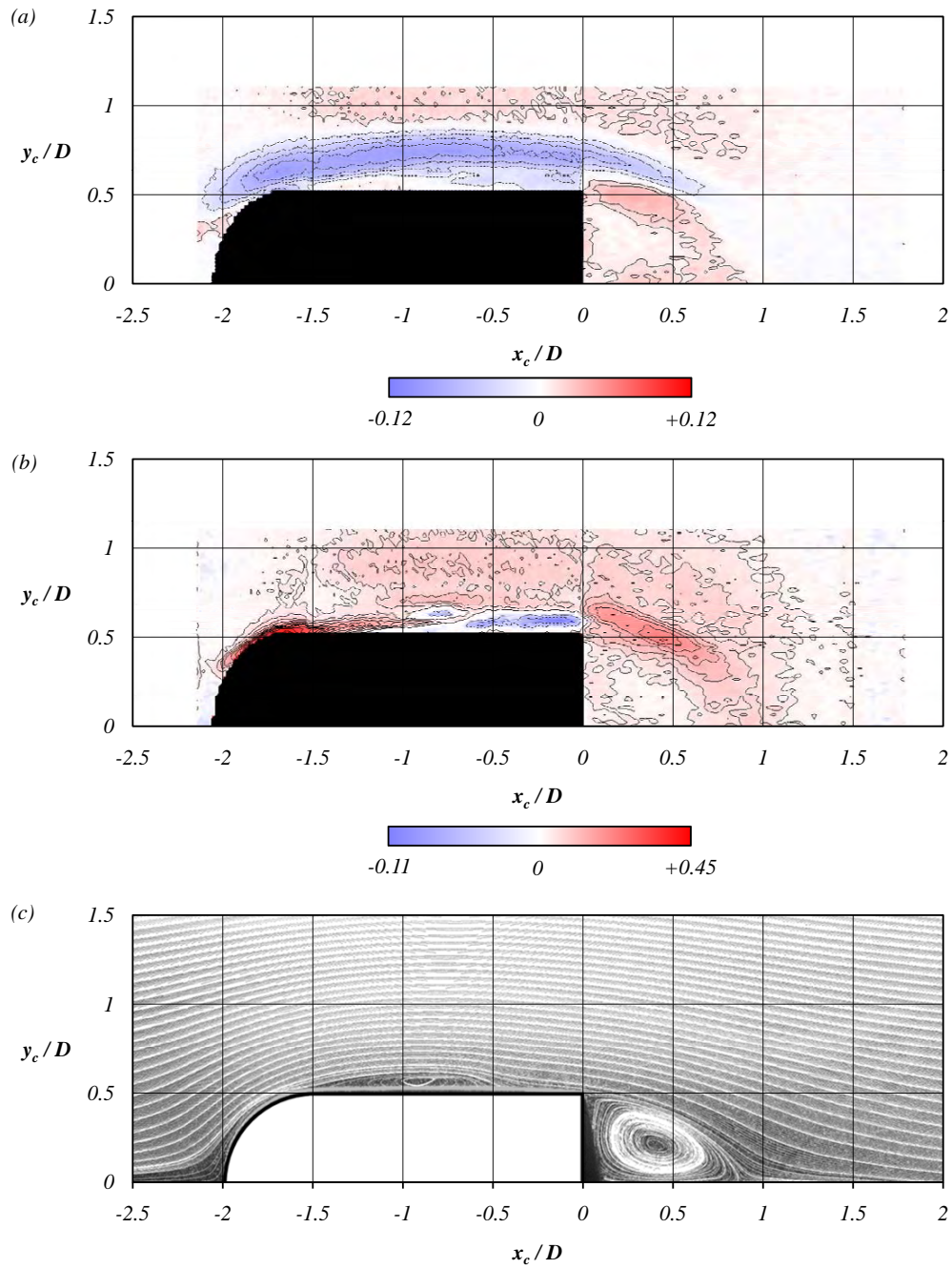


FIGURE 24. A complete map around the main cylinder for the  $d = 1\text{mm}$  control cylinder. Global mode frequency change  $\tilde{f}(x_c, y_c)$  is shown in (a) and the base pressure change  $\tilde{C}_{pb}(x_c, y_c)$  is shown in (b). The isolines are in the intervals of 0.01 for (a) and 0.03 in (b), continuous for positive and dashed for negative values. Blue color designates a decrease and red an increase in for both frequency and base pressure. Streamlines of mean velocity for the natural flow are given as reference in (c).

REFERENCES

- APELT, C. J. & WEST, G. S. 1975 The effects of wake splitter plates on bluff-body flow in the range  $10^4 \leq R \leq 5 \times 10^4$ . Part 2. *J. Fluid Mech.* **71**, 145–160.
- APELT, C. J., WEST, G. S. & SZEWCZYK, A. A. 1973 The effects of wake splitter plates on the flow past a circular cylinder in the range  $10^4 \leq R \leq 5 \times 10^4$ . *J. Fluid Mech.* **61**, 187–198.
- BEARMAN, P. W. 1965 Investigation of the flow behind a two-dimensional model with a blunt trailing edge and fitted with splitter plates. *J. Fluid Mech.* **21**, 241–255.
- BLOOR, M. S. 1964 The transition to turbulence in the wake of a circular cylinder. *J. Fluid Mech.* **19**, 290–304.
- CADOT, O., THIRIA, B. & BEAUDOIN, J.-F. 2009 Passive drag control of a turbulent wake by local disturbances. In *Unsteady Separated Flows and their Control* (ed. M. Braza & K. Hourigan), pp. 529–537.
- CHOMAZ, J.-M. 2005 Global Instabilities in Spatially Developing Flows: Non-Normality and Nonlinearity. *Ann. Rev. Fluid Mech.* **37**, 357–392.
- COUAIRON, A. & CHOMAZ, J. M. 1999 Fully nonlinear global modes in slowly varying flows. *Phys. Fluids* **11** (12), 3688–3703.
- CROUCH, J. D., GARBARUK, A., MAGIDOV, D. & TRAVIN, A. 2009 Origin of transonic buffet on aerofoils. *J. Fluid Mech.* **628**, 357–369.
- DALTON, C., XU, Y. & OWEN, J. C. 2001 The Suppression of Lift on a Circular Cylinder due to Vortex Shedding at Moderate Reynolds Numbers. *J. Fluid Structures* **15**, 617–628.
- FRANC, J.-P. & MICHEL, J.-M. 2005 *Fundamentals of Cavitation*. Springer.
- GERRARD, J. H. 1966 The mechanics of the formation region of vortices behind bluff bodies. *J. Fluid Mech.* **25**, 401–413.
- GIANNETTI, F. & LUCHINI, P. 2007 Structural sensitivity of the first instability of the cylinder wake. *J. Fluid Mech.* **581**, 167–197.
- GOUJON-DURAND, S., JENFFER, P. & WESFREID, J. E. 1994 Downstream evolution of the Bénard–von Kármán instability. *Phys. Rev. E* **50** (1), 308–313.
- HILL, D. C. 1992 A theoretical approach for analyzing the restabilization of wakes. *NASA Tech. Rep.* **92**, 29394.
- KUO, C.-H., CHIOU, L.-C. & CHEN, C.-C. 2007 Wake flow pattern modified by small control cylinders at low Reynolds number. *J. Fluid Structures* **23** (6), 938–956.
- LUCHINI, P., GIANNETTI, F. & PRALITS, J. 2008 Structural sensitivity of linear and nonlinear global modes. In *Proceedings of Fifth AIAA Theoretical Fluid Mechanics Conference, Seattle, Washington, AIAA Paper 2008-4227*.
- LUCHINI, P., GIANNETTI, F. & PRALITS, J. 2009 Structural Sensitivity of the Finite-Amplitude Vortex Shedding Behind a Circular Cylinder. In *Unsteady Separated Flows and their Control* (ed. M. Braza & K. Hourigan), pp. 151–160.
- MARQUET, O., SIPP, D. & JACQUIN, L. 2008 Sensitivity analysis and passive control of cylinder flow. *J. Fluid Mech.* **615**, 221–252.
- MITTAL, S. 2001 Control of Flow Past Bluff Bodies Using Rotating Control Cylinders. *J. Fluid Structures* **15**, 291–326.
- MITTAL, S. & RAGHUVANSHI, A. 2001 Control of vortex shedding behind circular cylinder for flows at low Reynolds numbers. *Int. J. Numer. Methods Fluids* **35**, 421–447.
- NORBERG, C. 2001 Flow around a circular cylinder: aspects of fluctuating lift. *J. Fluid Structures* **15**, 459–469.
- PAREZANOVIĆ, V. 2011 Experimental study of the sensitivity of global properties of turbulent bluff body wakes using steady disturbance methods. PhD thesis, Ecole Nationale Supérieure de Techniques Avancées de ParisTech.
- PAREZANOVIĆ, V. & CADOT, O. 2009a The impact of a local perturbation on global properties of a turbulent wake. *Phys. Fluids* **21** (7), 071701.
- PAREZANOVIĆ, V. & CADOT, O. 2009b Modulated global mode of a controlled wake. In *Advances in Turbulence XII* (ed. B. Eckhardt), pp. 217–220.
- PASTOOR, M., HENNING, L., NOACK, B. R., KING, R. & TADMOR, G. 2008 Feedback shear layer control for bluff body drag reduction. *J. Fluid Mech.* **608**, 161–196.
- PRALITS, J. O., BRANDT, L. & GIANNETTI, F. 2010 Instability and sensitivity of the flow around a rotating circular cylinder. *J. Fluid Mech.* **650**, 513–536.

- PRASAD, A. & WILLIAMSON, C. H. K. 1997 Three-dimensional effects in turbulent bluff-body wakes. *J. Fluid Mech.* **343**, 235–265.
- ROSHKO, A. 1954 On the drag and shedding frequency of two-dimensional bluff bodies. *N.A.C.A. Tech. Note* **3619**.
- SAKAMOTO, H. & HANIU, H. 1994 Optimum suppression of fluid forces acting on circular cylinder. *J. Fluids Eng.* **113**, 183–189.
- SAKAMOTO, H., HANIU, H. & TAN, K. 1991 An optimum suppression of fluid forces by controlling a shear layer separated from a square prism. *ASME Trans. J. Fluids Eng.* **113**, 183–189.
- STRYKOWSKI, P. J. & SREENIVASAN, K. R. 1985 The control of transitional flows. In *AIAA Shear Flow Control Conference*, pp. Paper 85–0559.
- STRYKOWSKI, P. J. & SREENIVASAN, K. R. 1990 On the formation and suppression of vortex ‘shedding’ at low Reynolds numbers. *J. Fluid Mech.* **218**, 71–107.
- THIRIA, B., CADOT, O. & BEAUDOIN, J.-F. 2009 Passive drag control of a blunt trailing edge cylinder. *J. Fluid Structures* **25**, 766–776.
- THIRIA, B., GOUJON-DURAND, S. & WESFREID, J. E. 2006 The wake of a cylinder performing rotary oscillations. *J. Fluid Mech.* **560**, 123–147.
- THIRIA, B. & WESFREID, J. E. 2007 Stability properties of forced wakes. *J. Fluid Mech.* **579**, 137–161.
- WILLIAMSON, C. H. K. 1996a Vortex dynamics in the cylinder wake. *Ann. Rev. Fluid Mech.* **28**, 477–539.
- WU, T. Y. T. 1972 Cavity and Wake Flows. *Ann. Rev. Fluid Mech.* **4**, 243–284.
- YILDIRIM, I., RINDT, C. C. M. & STEENHOVEN, A. A. 2010 Vortex dynamics in a wire-disturbed cylinder wake. *Phys. Fluids* **22** (9), 094101.
- ZIELINSKA, B. J. A. & WESFREID, J. E. 1995 On the spatial structure of global modes in wake flow. *Phys. Fluids* **7**, 1418–1424.